The International Journal of Advanced Manufacturing Technology (2019) 100:2401–2422
https://doi.org/10.1007/s00170-018-2879-8

ORIGINAL ARTICLE

Intermetallic compounds (IMCs) formation during dissimilar friction-stir welding of AA5005 aluminum alloy to St-52 steel: numerical modeling and experimental study

H. Aghajani Derazkola[1] · F. Khodabakhshi[2]

Received: 5 February 2018 / Accepted: 9 October 2018 / Published online: 16 October 2018

Abstract
In this research, AA5005-O aluminum-magnesium alloy and St-52 low carbon steel sheets were friction-stir welded in a butt-dissimilar joint design. Effects of different processing parameters including tool rotational speed (w), traverse velocity (v), plunge depth, and offset distance on the solid-state weldability of these dissimilar materials were assessed in terms of formation of intermetallic compound (IMC) layer at the interface. A 3D thermo-mechanical finite element modeling procedure was employed to predict the nucleation and growth of IMC layer. Formation of various FeAl, $FeAl_3$, and Fe_2Al_5 IMCs at the interface, layer morphology, and thickness were experimentally studied as well, by using X-ray diffraction (XRD) and field emission scanning electron microscopy (FE-SEM) analysis techniques. A good agreement between the simulated thermal results and experimental data was noticed. The results showed that the thickness of IMC layer at the interface as the main controlling parameter in transverse tensile property and fracture behavior of produced dissimilar joints can be varied extremely as a function of processing parameters. By decreasing the heat input and suppressing the kinetics of IMCs layer formation, the tensile performance of dissimilar welded joints is improved, considerably. However, the soundness of these dissimilar welds played another main role as a restriction mechanism against this trend. The maximum joining efficiency is attained around 90% at an optimized working window of $w = 1200$ rpm, $v = 90$ mm/min, and a plunge depth of 0.3 mm with an offset distance of 0.5 mm toward the Al side. The hardness of this optimized dissimilar weld is enhanced even more than the steel base metal caused by the formation of IMC layer at the interface as well as the dispersion of reinforcing intermetallic particles (IMPs).

Keywords Friction-stir welding · Dissimilar joint · AA5005-O aluminum alloy · St-52 steel · Intermetallic compounds (IMCs) · Thermo-mechanical simulation

1 Introduction

Friction-stir welding (FSW) as a newly modified and versatile solid-state joining technology invented by TWI has been broadly utilized for similar and dissimilar bonding of different metals and alloys as compared to fusion welding technologies due to lower temperature and avoiding from severe melting difficulty issues, such as solidification shrinkage and cracking, porosity, distortion, residual stress, oxidation, and other defects as well as the possible destructive phase transformations [1–5]. In this process, a non-consumable rotating tool is penetrated into the along sides of metal sheets to be joined, after frictional heating mainly imposed by tool shoulder, severe plastic rotating and forging actions leads to solidified materials transfer from leading to trailing edge, and by transferring the tool along the joint line, the sheets can be welded at solid-state in a temperature below than the melting points of base metals [6–10]. Among different metals/alloys combinations, innovative aluminum-steel bi-metallic structures possess good demands considering the strong interests according to the environmentally friendly, cost-effective, fuel efficiency, energy preservation, and lightweight concepts for modern vehicle/automotive industrial applications as well as the combination

✉ F. Khodabakhshi
fkhodabakhshi@ut.ac.ir; farzadkhodabakhshi83@gmail.com

[1] Young Researchers and Elites Club, Science and Research Branch, Islamic Azad University, Tehran, Iran

[2] School of Metallurgical and Materials Engineering, College of Engineering, University of Tehran, P.O. Box: 11155-4563, Tehran, Iran

of various properties [11–15]. In a new desire development for engine cradles of Honda Motor Company, an Al-Fe lap joint connection would be required, as an instance for automobile application. However, attributing to large differences between the physical, chemical, and mechanical properties of these two kinds of dissimilar metals, it is very difficult to overcome the related difficulties during their dissimilar joining with traditional welding processes [13, 15, 16]. Thus, FSW as a promising process for this aim has emerged and attracted significant attention [16–19]. Meanwhile, it is still challenging to accomplish this dissimilar joining between aluminum and steel alloys by FSW process, due to formation of hard and brittle intermetallics at the interface as induced by the thermodynamically un-avoidable solid-state chemical reactions and their detrimental influences on the mechanical property, as well as keeping the grains and precipitates structures for aluminum base alloy during stirring process and subsequent temperature increasing [16, 20–25].

In various researches [20–23, 26–31], dissimilar friction-stir weldability of aluminum alloys and different steels were examined. Joining of the AA6061 aluminum alloy to AISI 1018 was successfully accomplished by FSW process in the work of Jiang et al. [32] and Chen et al. [33] by fabrication of a defect-free weld with good quality and admirable tensile strength. Effect of tool plunge depth on the strength of the dissimilar joint between commercial pure aluminum and low carbon steel was reported in the research of Elrefaey et al. [34]. AA6013-T4 aluminum alloy and X5CrNi18-10 stainless steel were friction-stir welded by Uzun et al. [35]. In the work of Watanabe et al. [36], the effects of processing parameters (tool rotational speed and probe offset distance) on the microstructure and mechanical performance of dissimilar FSWs between an AA5083 alloy and SS400 mild steel were studied. A maximum tensile strength improvement up to ~ 90% of the aluminum base alloy was reported. Chen [37] did the same parametric study between AA6061-T651 alloy and low carbon steel with a maximum tensile strength of ~ 75%. By controlling the intermetallics formation in another parametric study, Dehghani et al. [38] reported a joint strength of ~ 90% for dissimilar FSW between an Al-Mn alloy and mild steel. In the work of Haghshenas et al. [16], reducing the welding traverse velocity showed an impact influence on the mechanical property of dissimilar FSWs between AA5754 aluminum alloy with DP600 and 22MnB5 steels. During dissimilar joining of AA6061-T6 aluminum alloy and TRIP steel by Liu et al. [39], changes in the composition, morphology, and thickness of intermetallic compounds (IMCs) layer at the interface by varying of processing parameters were found very effective. Ratanathavorn et al. [40] showed the bonding mechanism between AA5754 aluminum alloy and DP800 steel as the formation of a ~ 2-μm-thick IMC layer at the interface aided by the interfacial diffusion reactions. Multi-passes friction-stir welding was introduced by Leitao et al. [41] to avoid the discontinuities by increasing the bonding path. The effects of zinc inter-layer on the formation and characteristics of dissimilar friction-stir welds between aluminum and steel sheets were investigated in the works of Dong et al. [42] and Zheng et al. [43], by utilizing the galvanized steel as one substrate. The results showed the importance of ZnO formation on the joint strength and fracture behavior of dissimilar welds. Huang et al. [44] introduced the self-riveting friction-stir welding as an effective process for joining of AA6082-T6 aluminum alloy and QSTE340TM steel with the enhanced mechanical property. In two recent works by Yazdipour et al. [21] and Rafiei et al. [23], dissimilar friction-stir welding between Al-Mg alloys and A316L stainless steel in a butt-joint design was investigated. Processing parameters were optimized to attain a joint strength ratio higher than 90%.

Thermo-mechanical simulation of FSW process is very interesting and valuable to predict the temperature profile, materials flow pattern, and flow/residual stress distributions by considering the simultaneous couple influences of heat flow, severe plastic mixing, and visco-plastic flow behavior of deformed materials depending on the processing temperature [45, 46]. Although several works have been conducted on the dissimilar FSW of Al-Fe bi-metallic joints, there is only one report about thermo-mechanical modeling of aluminum to steel friction-stir welding in the literature by Tang et al. [22]. In that study, they have simulated the effects of pre-heating treatment on the temperature and materials flow profiles during FSW of E235A steel and AA6061 aluminum alloy [22]. The results showed that the pre-heating can increase peak temperature, improve the plastic material flow velocity, and change the fracture mode of processed dissimilar welds. Formation of intermetallic compounds (IMCs) layer from Al-rich ($FeAl_3$, Fe_2Al_5) or Fe-rich (FeAl, Fe_3Al) complexes at the Al-Fe joint interface during FSW process has a detrimental influence on the mechanical performance of dissimilar welds due to the brittleness nature of IMC layer and its high hardness [20, 21, 26, 47–50]. The kinetics of this IMC layer growth at the interface as caused by in situ solid-state chemical interfacial reactions is a lattice diffusion-controlled phenomenon depending on the imposed thermo-mechanical history during the process [20, 21, 26, 49–53]. Therefore, the main object/novelty of the present research is to study the formation, morphological characteristics, and growth of the IMC layer at the Al-Fe interface during the FSW process by thermo-mechanical modeling. For this aim, sheets of an AA5005 Al-Mg alloy and an St-52 low carbon steel were friction-stir welded at various combinations of processing conditions with a butt-joint design. These two materials are used for industrial applications in food equipment, storage tanks, and home appliances owing to their superior corrosion resistance and mechanical property, respectively [54, 55]. In addition to three-dimensional finite element simulation, the effects of tool rotational speed (w), traverse velocity (v),

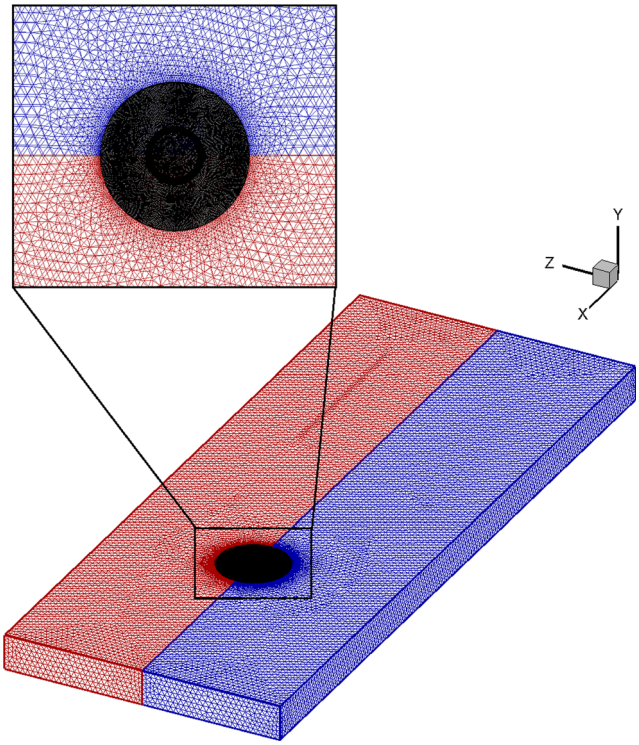

Fig. 1 A schematic representation for mesh structure employed in this research for modeling of the dissimilar joining between aluminum and steel with lap-design

forging plunge depth, and probe offset distance as the main processing parameters on the microstructural features, indentation hardness, tensile strength, and fracture behavior of dissimilar welded joints were assessed. Finally, the processing parameters were optimized based on the thickness and morphology of formed IMC layer at the interface as well as the soundness of weldments and its subsequent influence on the joining efficiency during transverse tensile testing.

2 Governing equations and process modeling

Heat generation and materials flow velocity field during friction-stir welding are mainly caused by a thermo-mechanical process due to coupled effects of contact friction and severe plastic deformation by the stirring action of the rotating tool [56]. To consider both of these two

Table 1 Chemical compositions of the examined AA5005-O aluminum alloy and St-52 low carbon steel

Base metal	Elements								
	Al	Fe	C	Cr	Mg	Mn	Cu	Zn	Si
AA5005-O	Base	0.60	–	0.07	1.10	0.05	0.12	0.20	0.20
St-52	–	Base	0.20	0.30	–	0.80	0.30	–	0.50

Table 2 Mechanical properties of base metals: yield stress (σ_y, MPa), ultimate tensile strength (σ_{UTS}, MPa), elongation to failure (e, %), and Vickers hardness (HV)

Material	σ_y	σ_{UTS}	E	HV	Melting point
AA5005-O	41.5	124	20	75	630 °C
St-52	355	580	25	235	1400 °C

interconnection effects during hot deformation to predict the formation of an aluminum-steel bi-metallic joint during FSW process, a three-dimensional ANSYS/explicit finite element model based on the combination of the thermal analysis and plastic material flow, by assumption of a density-based non-Newtonian fluid with visco-plastic flow behavior for these dissimilar base metals, can be employed [57]. The meshed model for this aim is shown in Fig. 1. As indicated, the frustum tungsten carbide tool and both of aluminum and steel workpieces were covered by using the tetrahedral/hybrid elements with T-grid combination shape and adaptive mesh generation system. As it is well established, the 3D non-linear heat transfer equation by considering an internal heat source (Q_{Total}) in a spatial Cartesian coordinate (x, y, z) can be expressed as follows [58]:

$$k\left(\frac{\partial^2 T}{\partial x^2}+\frac{\partial^2 T}{\partial y^2}+\frac{\partial^2 T}{\partial z^2}\right)+Q_{\text{Total}}=\rho c\frac{\partial T}{\partial t} \quad (1)$$

where ρ is the density of materials, c is the mass-specific heat capacity, and k is the coefficient of thermal conductivity [59]. All convection and radiation boundary conditions for solving this heat transfer equation considering the real condition can be explained as follows [60, 61]. The main physical properties of the AA5005 alloy can be defined in a thermal function as below [62]:

$$c_p = 911.2{-}0.605T + 1.77\times 10^{-3}T^2{-}3.09\times 10^{-8}T^3 \quad (2)$$

Fig. 2 The implemented experimental set-up

Table 3 The examined combinations of processing parameters for dissimilar FSW

Tool factors	Levels
Rotational speed (rpm)	920, 1000, and 1200
Traverse velocity (mm/min)	54 and 90
Plunge depth (mm)	0.1, 0.3, and 0.6
Tilting angle (degree)	2
Offset distance	0.5 and 1.5 mm toward the Al side and 1.5 mm toward the steel side

$$k = 25.2 + 0.398T + 7.36 \times 10^{-6}T^2 - 2.52 \times 10^{-7}T^3 \quad (3)$$

and as the same as for the St-52 low carbon steel as below [62]:

$$c_p = 462 - 8.1T + 3.2 \times 10^{-4}T^2 + 2.0 \times 10^{-7}T^3 \quad (4)$$

$$k = 3.7 + 0.09T - 1.8 \times 10^{-4}T^2 + 7.8 \times 10^{-8}T^3 \quad (5)$$

and finally for the tungsten carbide tool with the following description equations [62].

$$c_p = 128.3 - 3.279 \times 10^{-2}T + 4.31 \times 10^{-6}T^2 \quad (6)$$

$$k = 153.5 - 9.56 \times 10^{-2}T + 5.23 \times 10^{-5}T^2 \quad (7)$$

To solve this 3D heat conduction problem, the three-dimensional Cartesian coordinate system was employed and the initial and boundary conditions considered in this model were based on the real physical conditions as follows. The generated heat at the tool shoulder/workpiece interface can be defined as follows [59]:

$$Q_{ss} = [\delta\tau + (1-\delta)\mu P]\frac{2}{3}\pi\omega\left(R_1^3 - R_1^2\right) \quad (8)$$

where δ denotes the spatially variable fractional slip between the tool and workpiece interface, which is $0 \le \delta \le 1$ range ($\delta = 0$ in pure sliding and $\delta = 1$ in pure sticking condition). μ is the friction coefficient which can consider as 0.5–0.64 for the polymer/steel contact interface and 0.3–0.45 for the aluminum/steel one, respectively [57, 58]. The τ is maximum shear stress which is equal to $\sigma_y/\sqrt{3}$ [58], where σ_y is the material yield stress.

Under the bottom surface of sheets, there was a backing plate at the actual condition and the heat transfer coefficient from the bottom of the workpiece was not the same as for free convection. The value of the heat transfer coefficient at the bottom surface of the workpiece can be determined as below [60, 61]:

$$k\left.\frac{\partial T}{\partial Z}\right|_{\text{Bottom}} = h_b(T - T_a) \quad (9)$$

where h_b is the bottom heat transfer coefficient and T_a is the ambient temperature (~298 K). The heat transfer coefficient at the bottom face can be varied depending on the local temperature and is given by the following relation [60, 61]:

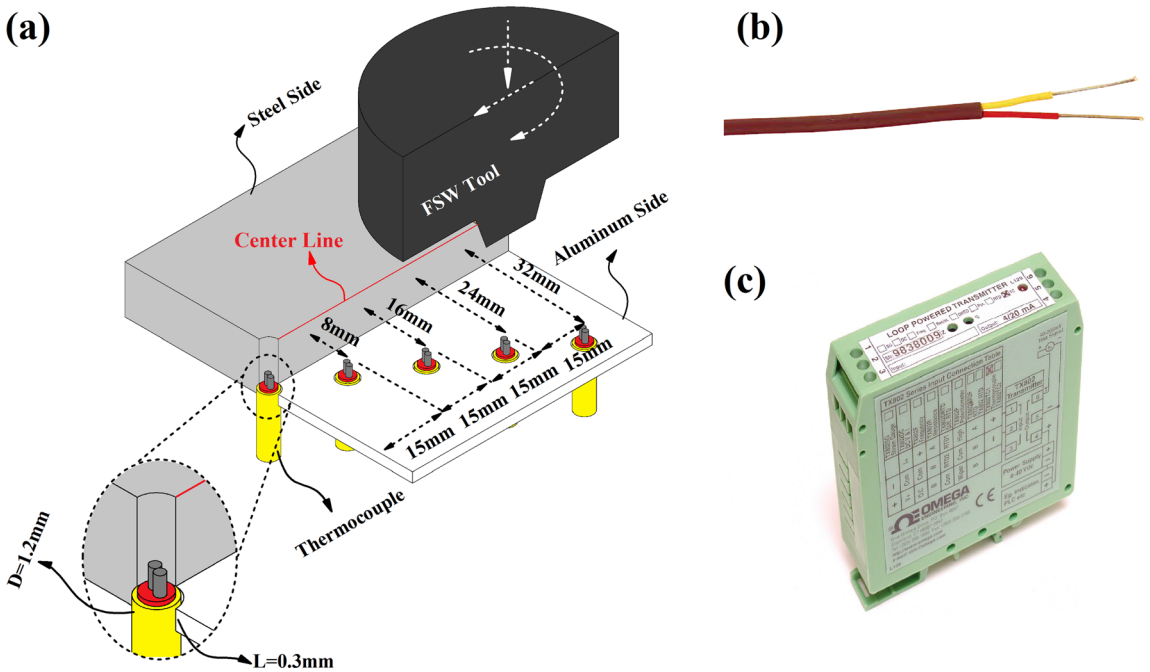

Fig. 3 **a** Schematic plot for pre-placing of thermocouples during the friction-stirring process and their positions to monitor the thermal profiles, **b** *K*-thermocouple wire, and **c** thermocouple transmitter for recording the input data

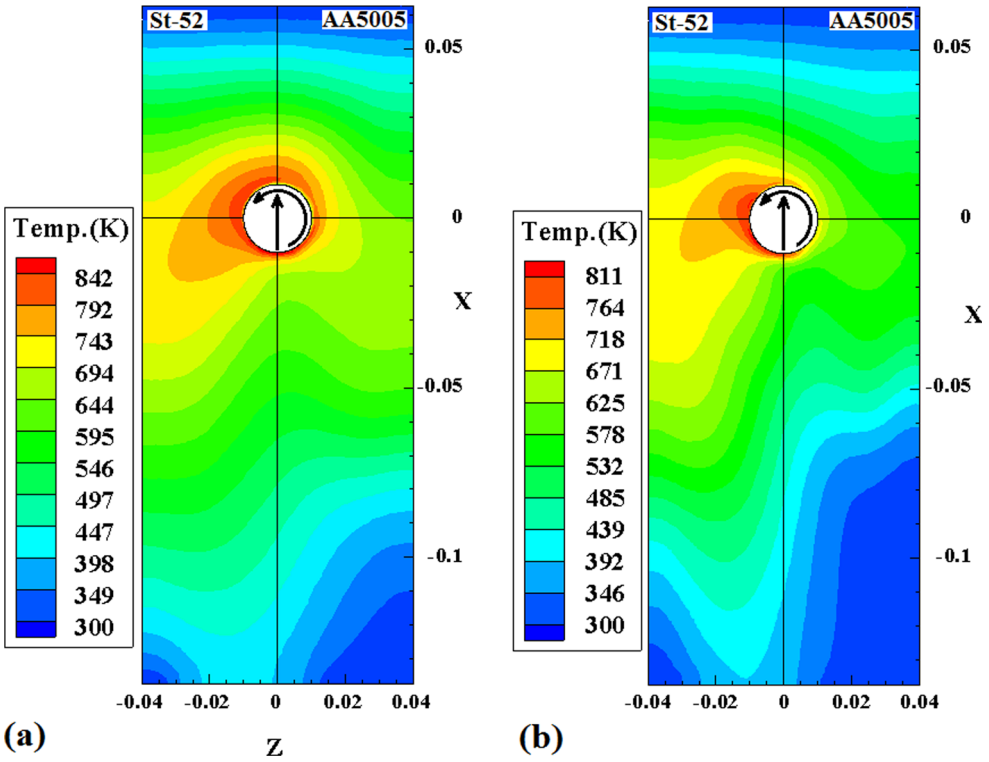

Fig. 4 Simulated temperature contours on the surface of dissimilar AA5005/St-52 welds at different tool rotational speeds of **a** 920 and **b** 1200 rpm with a constant traverse velocity of 54 mm/min

$$h_b = h_{b0}(T - T_a)^{0.25} \quad (10)$$

where h_{b0} is the heat transfer parameter for the bottom surface. As Eq. (10) shows, this parameter is a constant and it has a different unit than the heat transfer coefficient which is spatially variable. At the top surface, heat transfer is mainly due to both of convection and radiation phenomena as given by the following equation [60]:

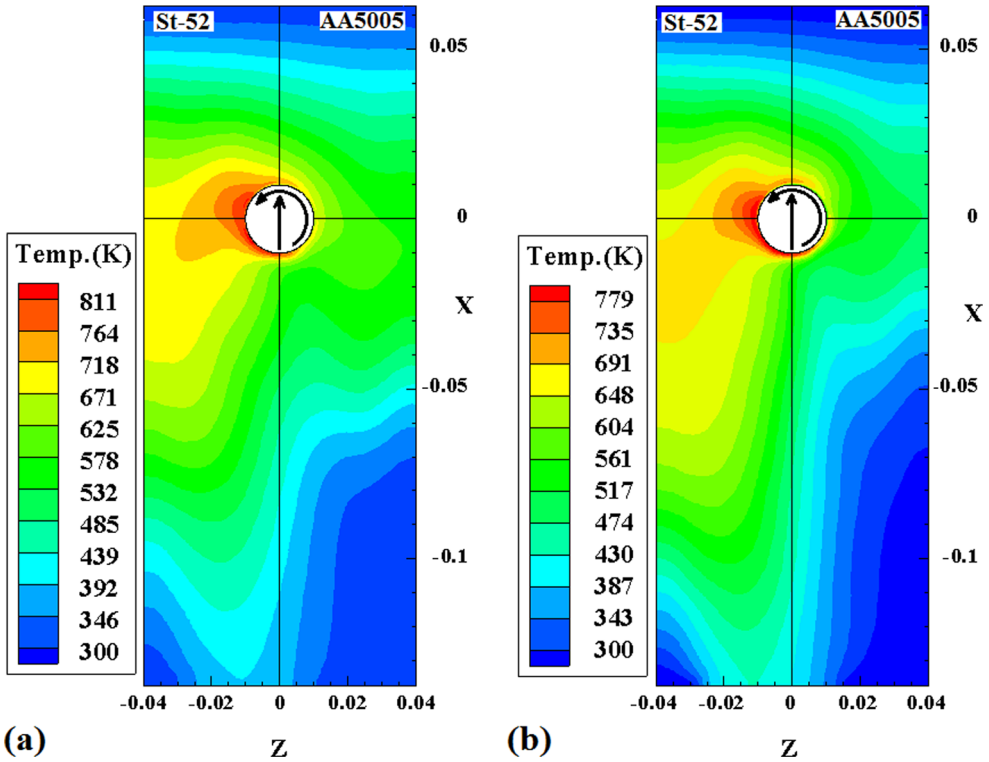

Fig. 5 Simulated temperature contours on the surface of dissimilar AA5005/St-52 welds at different tool traverse velocities of **a** 54 and **b** 90 mm/min with a constant rotational speed of 920 rpm

$$-k\left.\frac{\partial T}{\partial Z}\right|_{\text{Top}} = B\varepsilon\left(T^4 - T_a^4\right) + h_t(T - T_a) \tag{11}$$

where B is the Stefan–Boltzmann constant (5.67×10^{-16} J K^{-4} m^{-2} s^{-1}), ε is the thermal emissivity, and h_t is the convective heat transfer coefficient at the top surface. The computed temperature values were found to be insensitive to the values of h_t and its value was taken as zero for simplicity. At the all other surfaces, temperatures were set to be the ambient value (298 K). Between warm-up after pin-insertion and pin-extraction from the workpiece, the thermal cycles at different locations assume equidistant from the weld center line. Therefore, the temperature and velocity fields can be solved with the assumption of a steady-state behavior.

Based on the momentum conservation principle, the plastic material velocity field in the Cartesian coordinates of (x, y, z) and index notation of $(i, j) = (1, 2, 3)$ can be described according to the following relation [60, 61]:

$$\rho\frac{\partial u_i \partial u_j}{\partial x_i} = -\frac{\partial P}{\partial x_j} + \frac{\partial}{\partial x_i}\left(\mu\frac{\partial u_i}{\partial x_j} + \mu\frac{\partial u_j}{\partial x_j}\right) - \rho U_1\frac{\partial u_j}{\partial x_1} \tag{12}$$

where in this equation, u is the velocity vector, U_1 is the welding traverse velocity, P is the welding pressure, and μ is the non-Newtonian viscosity [60, 61]. This viscosity factor can be expressed as a function of flow stress (σ_e) and effective strain rate ($\dot{\varepsilon}$) as below [62]:

$$\mu = \frac{\sigma_e}{3\dot{\varepsilon}} = \frac{1}{3\alpha\dot{\varepsilon}}\operatorname{arcsinh}\left(\frac{Z}{A}\right)^{\frac{1}{n}} = \frac{1}{3\alpha\dot{\varepsilon}}\operatorname{arcsinh}\left(\frac{\dot{\varepsilon}\exp\left(\frac{Q}{RT}\right)}{A}\right)^{\frac{1}{n}} \tag{13}$$

where α, A, and n are the material constants, Z is the Zener–Hollomon parameter, Q is the temperature-independent activation energy, R is the universal gas constant, and T is the processing temperature [60]. To consider the intermixing effects between AA5005 alloy and St-52 steel base metals during dissimilar friction-stir bonding, a Eulerian solution approach with adaptive meshing system was used. The common faces were replaced with the virtual interface. These two 3D thermal and velocity field equations were solved simultaneously by the assumption of steady-state behavior to predict the temperature and materials flow profiles.

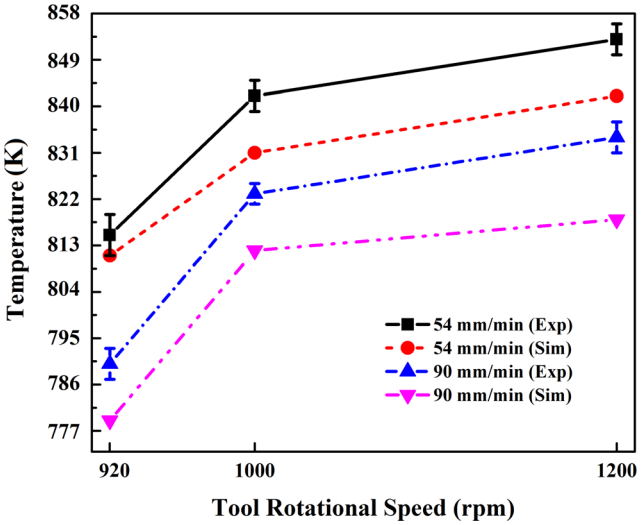

Fig. 7 Comparison between the effects of tool rotational speed and traverse velocity on the peak temperature of thermal cycles

3 Materials and research methods

In this work, AA5005-O aluminum alloy and St-52 steel plates with the thickness of 4 mm were cross-sectioned into

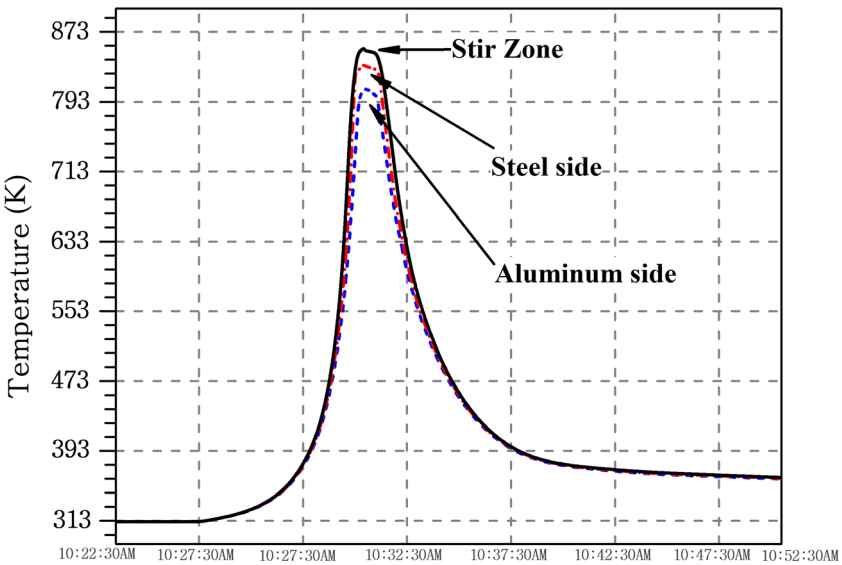

Fig. 6 Recorded thermal cycles at different sides and nugget zone during dissimilar friction-stir welding of AA5005 and St-52 alloys

Table 4 Comparison between the simulated and experimentally measured peak temperatures at various combinations of FSW processing parameters

	FSW tool parameters					
Peak temperature	$\omega = 920$ rpm		$\omega = 1000$ rpm		$\omega = 1200$ rpm	
	$v = 54$ mm/min	$v = 90$ mm/min	$v = 54$ mm/min	$v = 90$ mm/min	$v = 54$ mm/min	$v = 90$ mm/min
Experimental	815 K	790 K	842 K	823 K	853 K	834 K
Simulation	811 K	779 K	831 K	812 K	842 K	818 K
$\frac{T}{T_m}(AA5005)$	86%	82%	90%	87%	92%	89%
$\frac{T}{T_m}(St{-}52)$	38.7%	36.9%	40.6%	39.2%	41.4%	40%

the small samples with the length of 150 mm and width of 50 mm. These base metals (BM) with chemical composition and mechanical properties as reported in Tables 1 and 2, respectively were considered for the aim of dissimilar friction-stir welding. According to the expressed data in Table 2, a large difference (4 to 5 times) between the tensile strength and hardness of the aluminum (124 MPa and 75 HV) and steel base metals (580 MPa and 235 HV) is noticeable. Therefore, the dissimilar solid-state joining of them would be very challenging due to completely unlike material flow capability. All experiments were conducted in a butt-joint design by using a high energy milling machine system in a position control mode. A flexible clamping system made of high carbon steel was designed to clamp the plates in their proper positions during the process. These single-pass friction-stir butt-welds were performed by utilizing an FSW tool made of tungsten carbide (WC). This tool was designed with a shoulder diameter of 20 mm containing a conical probe with the length of 3 mm and diameters of 4 to 6 mm. Figure 2 shows the employed experimental set-up for the accomplishment of the FSW process. As expressed in Table 3, a wide combination for various processing parameters was assessed to found a

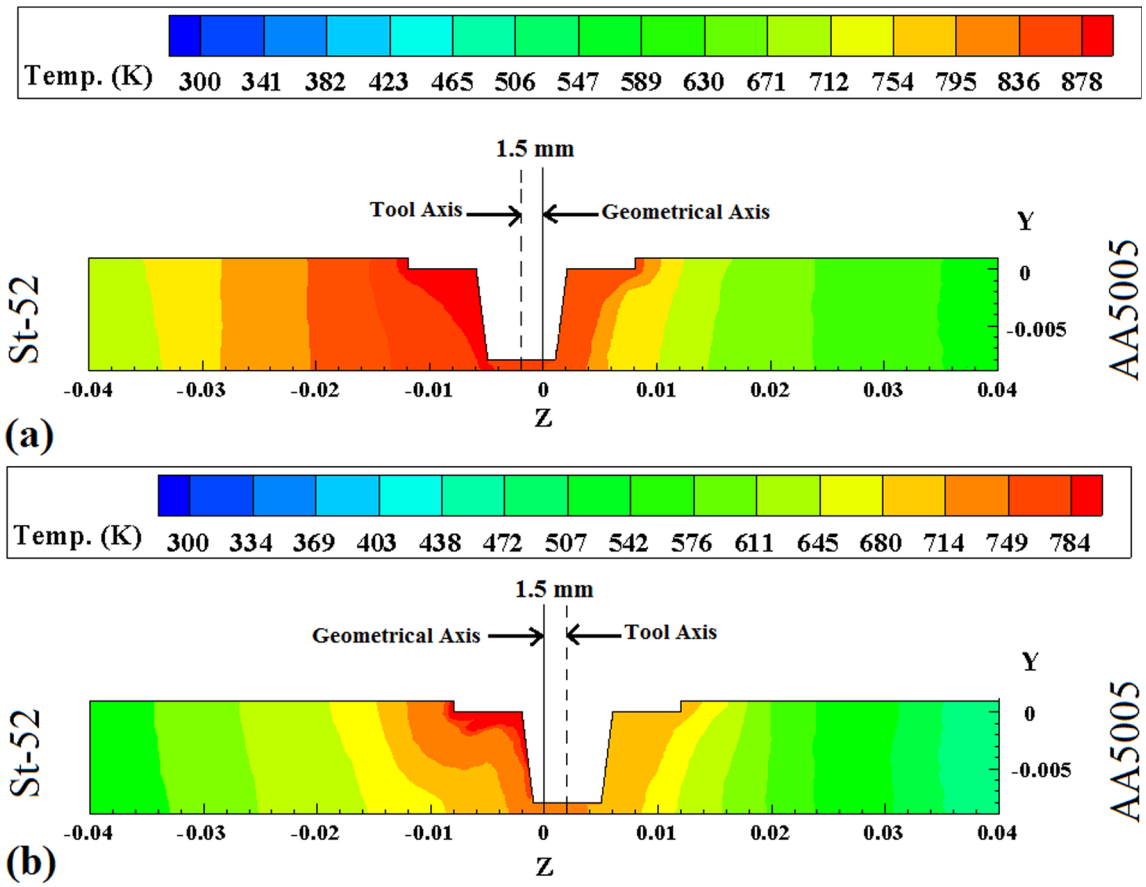

Fig. 8 Internal temperature profile contours for dissimilar FSWs at $w = 920$ rpm and $v = 54$ mm/min with a 1.5-mm tool offset toward the **a** aluminum and **b** steel sides, respectively

suitable working window, including tool rotational speed (w) at the constant values of 920, 1000, and 1200 rpm; traverse velocity (v) with the constant values of 54 and 90 mm/min; tool plunge depth at the constant values of 0.1, 0.3, and 0.6 mm; tool tilting angle of 2°; and tool offset distance with the constant values of 0.5 and 1.5 mm toward the Al and steel sides. To elaborate the effects of a given processing parameter, an experimental design of a single factor was conducted by varying that parameter and keeping the other ones constant.

Real thermal histories (temperature-time heating cycles) during FSW process were monitored by placing a *K*-type thermocouple inside the different regions of aluminum- and steel sides as well as the stirred zones, as schematically presented in Fig. 3. As seen, the position for pre-placing of *K*-thermocouples was outside of the mixed region during the FSW process. Actually, in this project, the aim of this thermal monitoring was only to measure some experimental data about the temperature profile/thermal cycle to compare with the modeling outputs. The location for pre-placing of *K*-thermocouple wires was not mattered, and only the measured data must be compared with the predicted values from the same locations. Therefore, to avoid contact of FSW tool with the thermocouple wires and scattering in the monitored data, it was decided to do the touching between wires and substrates at some locations outside of weld nugget. The prepared dissimilar welds were sectioned perpendicular to the FSW direction across the thickness section by using electrical discharge machining (EDM) technique. Thereafter, the standard metallographic sample preparation procedure was accomplished on the thickness cross-section of samples by grinding on the different grades of emery SiC papers followed by mechanical polishing on the diamond pastes down to the size of ~ 1 μm. To study the soundness of dissimilar welds cross-sections as well as the general material flow structure and formation of intermetallic compounds (IMCs) layer at the Al/Fe interface, field emission scanning electron microscopy (FE-SEM, VEGA//TESCAN-XMU, Russia) analysis was performed on the polished samples. The microscope was equipped with an energy dispersive X-ray spectroscopy (EDS) detector to do the elemental chemical analysis. X-ray diffraction (XRD) analysis was performed on the prepared thickness cross-sections, as well, by using a Philips X-ray diffractometer and *Cu-Kα* radiation, to characterize

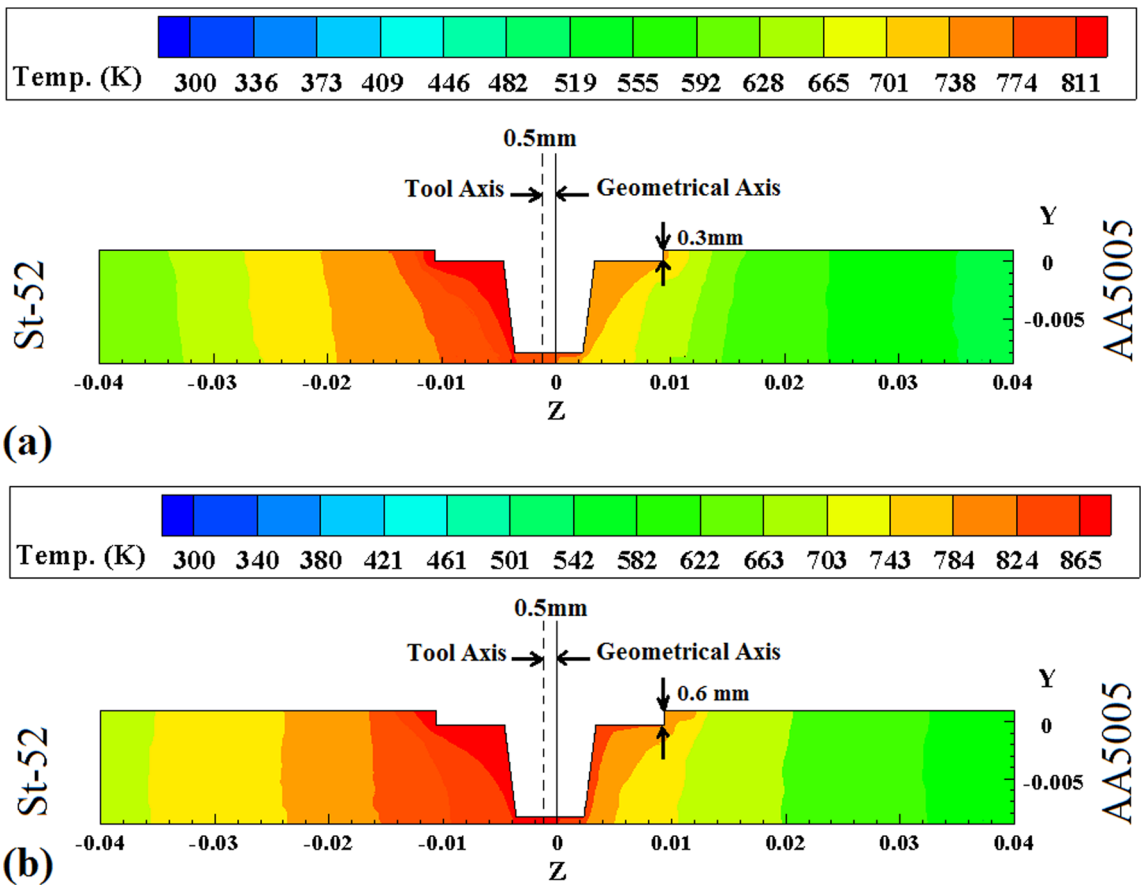

Fig. 9 Effects of **a** 0.3 and **b** 0.6 mm tool plunge depths on the internal thermal contours for the processed dissimilar FSWs at $w = 920$ rpm and $v = 54$ mm/min with a tool offset distance of 0.5 mm toward the steel side

the possible phase transformations. Mechanical performance of the processed dissimilar welds was evaluated during transverse tensile testing perpendicular to the FSW direction. Flat dog-bone shape tensile specimens were prepared from the processed dissimilar welds according to the ASTM: E8M-13 Standard by using the EDM technique. Testing was conducted by using a SANTAM Universal Tensile Testing Machine with a constant cross-head speed of 2 mm/min. For each condition, tensile tests were repeated three times and average joining efficiency values reported. Fracture behavior of dissimilar welds during transverse tensile testing was studied in terms of fracture location by visual macro-investigation of failed samples. Indentation Vickers macro-hardness testing was performed across the different regions of base metal (BM), heat-affected zone (HAZ), thermo-mechanical affected zone (TMAZ), and stir zone (SZ) for both of aluminum and steel sides. Measurements were carried out with 1 mm intervals from the bottom, middle, and top regions of dissimilar welds by using a Buhler micro-indenter machine (Buhler, Germany), an applied load of 200 g, and a dwell time of 15 s.

4 Results and discussion

4.1 Thermo-mechanical modeling results

It is well established that one of the main factors which can control the formation and growth of IMC layer during FSW of aluminum and steel is frictional heating as well as the plastic deformation [20, 47, 49]. Therefore, the temperature and materials flow fields were predicted by using finite element modeling at first to establish a correlation between them and the IMC layer at the interface. Effects of tool rotational speed and traverse velocity on the temperature profiles for the dissimilar friction-stir welded AA5005/St-52 joints are presented in Figs. 4 and 5, respectively. As expected, these predicted top surface temperature profiles at the steady-state conditions show that the maximum temperature is mainly from SZ toward the steel side and this peak value is enhanced with increasing the tool rotational speed and decreasing the traverse velocity. Figure 6 shows the real recorded temperature-time curves for the stirred region, aluminum, and steel sides of processed dissimilar

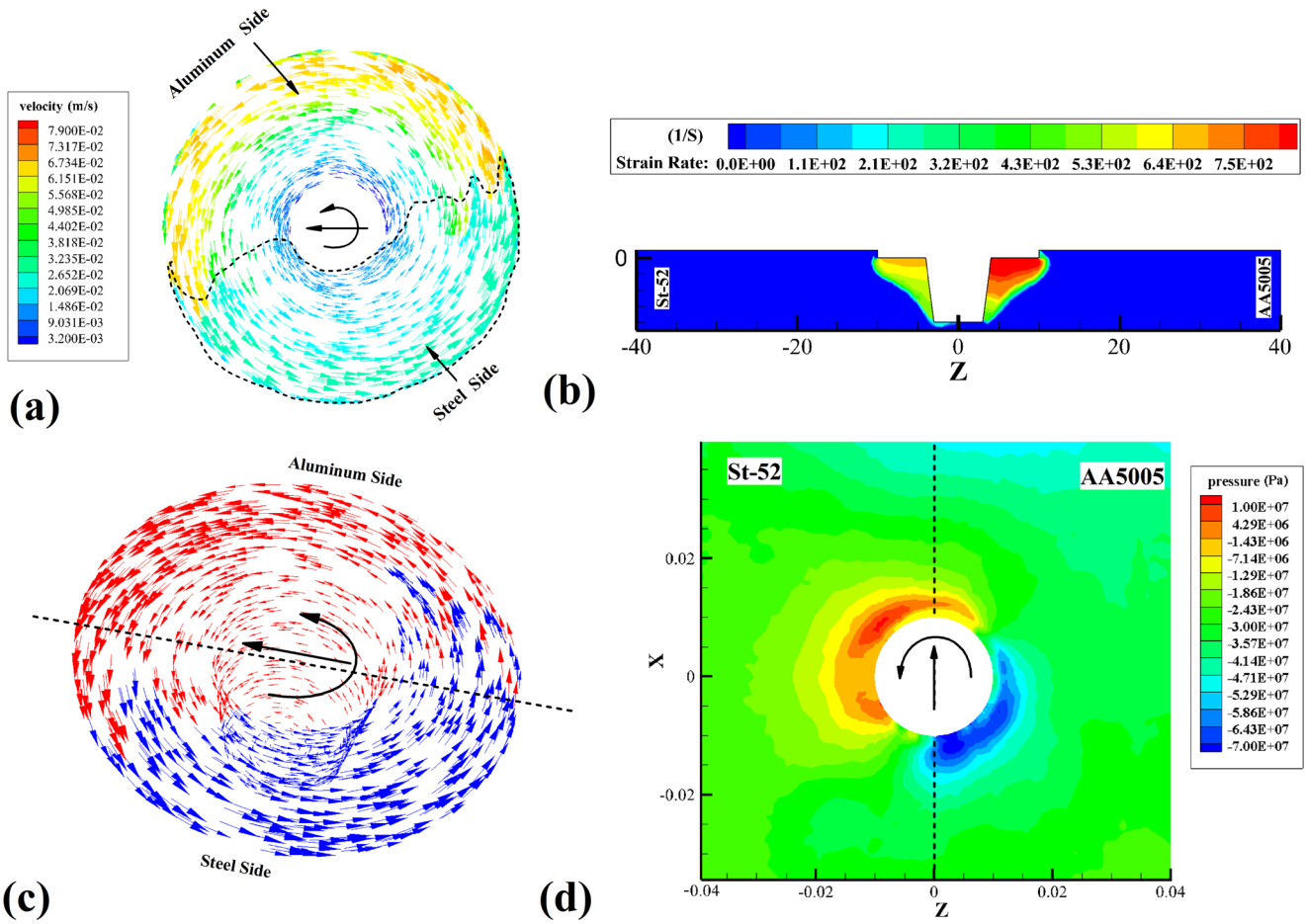

Fig. 10 The related **a** material velocity, **b** strain rate, **c** material distribution, and **d** flow stress contours for the dissimilar welded joint at $w = 920$ rpm and $v = 54$ mm/min with a tool plunge depth of 0.3 mm and an offset distance of 0.5 mm toward the aluminum side

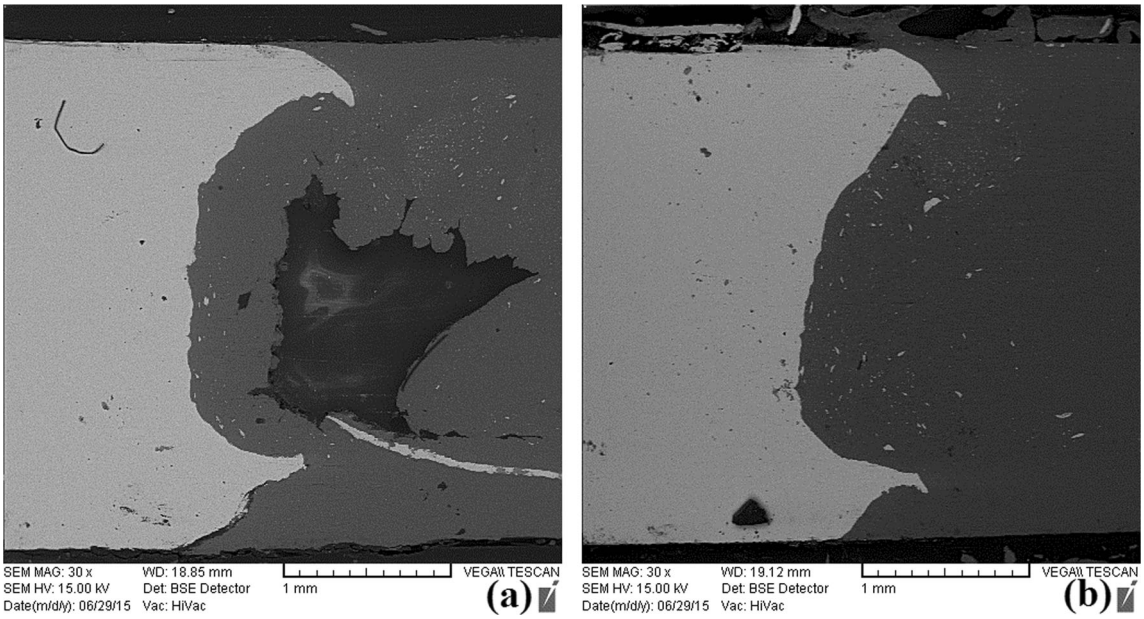

Fig. 11 FE-SEM macro-images showing the cross-sectional materials flow profiles for dissimilar FSW joints at different tool rotational speeds of **a** 920 and **b** 1200 rpm with a constant traverse velocity of 54 mm/min

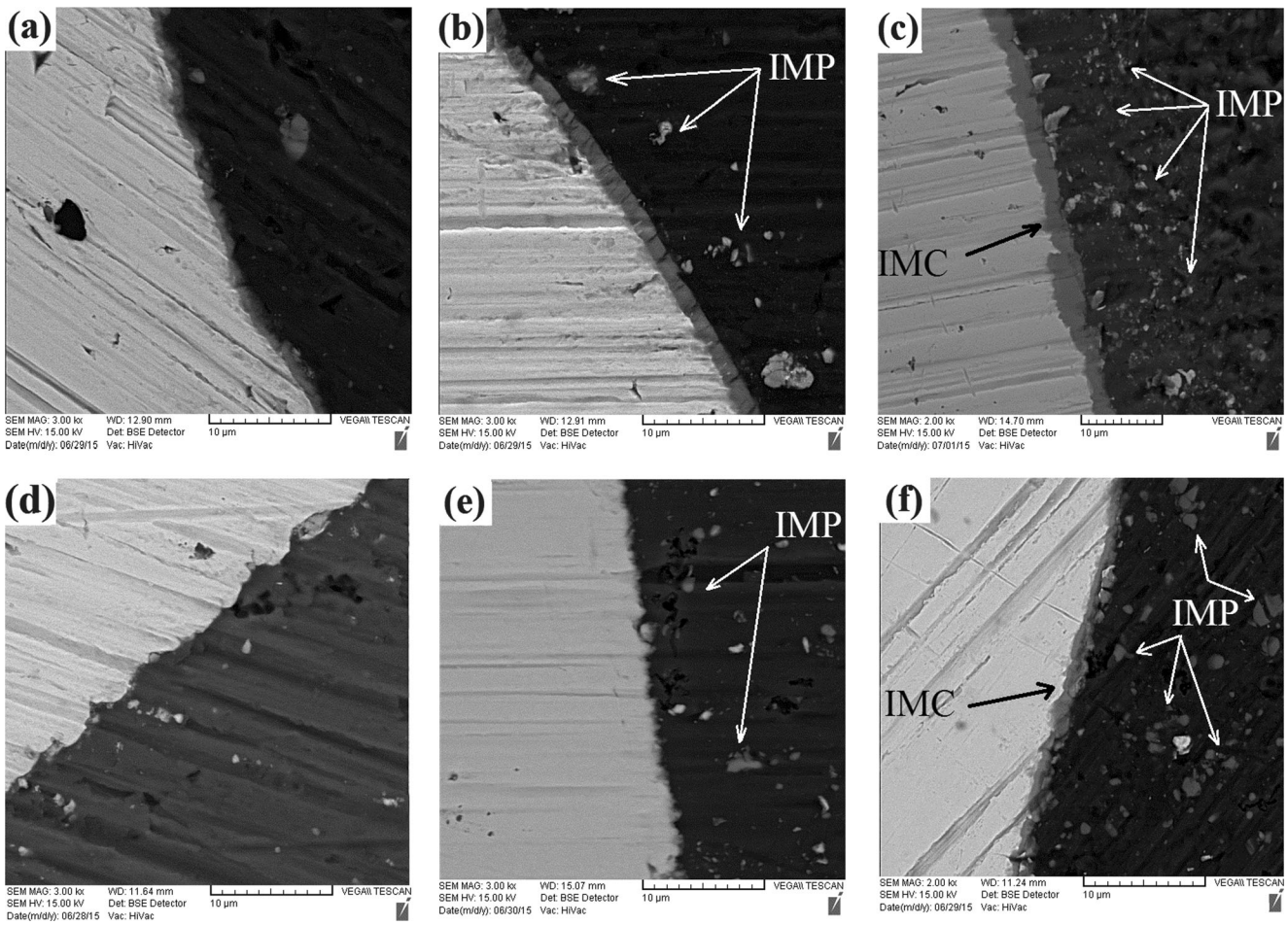

Fig. 12 FE-SEM images from the Al/Fe interfaces for the **a**–**c** upper and **d**–**f** lower parts of dissimilar welded joints at **a**, **d** $w = 920$, **b**, **e** $w = 1000$, and **c**, **f** $w = 1200$ rpm with $v = 54$ mm/min

welds. As seen, the highest peak temperature is inside the mixed region. In Fig. 7, the effects of main processing parameters (w and v) on the peak temperature for both of predicted and real measured profiles are compared. Also, these simulated and experimentally measured peak temperatures at the examined combination ranges of FSW parameters are quantitatively compared in Table 4. Furthermore, the differences between these peak temperatures and the melting temperatures of AA5005 and St-52 base alloys in terms of the ratio are calculated and expressed in Table 4, as well. As shown, for all conditions the simulation temperature is always lower than the experimental value with small deviations (good agreement) due to modeling assumptions or inaccuracy in monitoring the real temperature. The error between the experimental and simulation results is varied in the range of 10–20 K (1–3%).

As obvious, tool rotational speed has a more significant influence on the peak temperature for both of simulation and practical results, as compared to the traverse velocity. It can be due to the less dissipation of energy as well as the higher frictional heating and more plastic deformation [1, 2, 59]. The maximum processing peak temperature was about ~ 853 K and attained at a parameter of $w = 1200$ rpm and $v = 54$ mm/min. The effect of probe offset distance

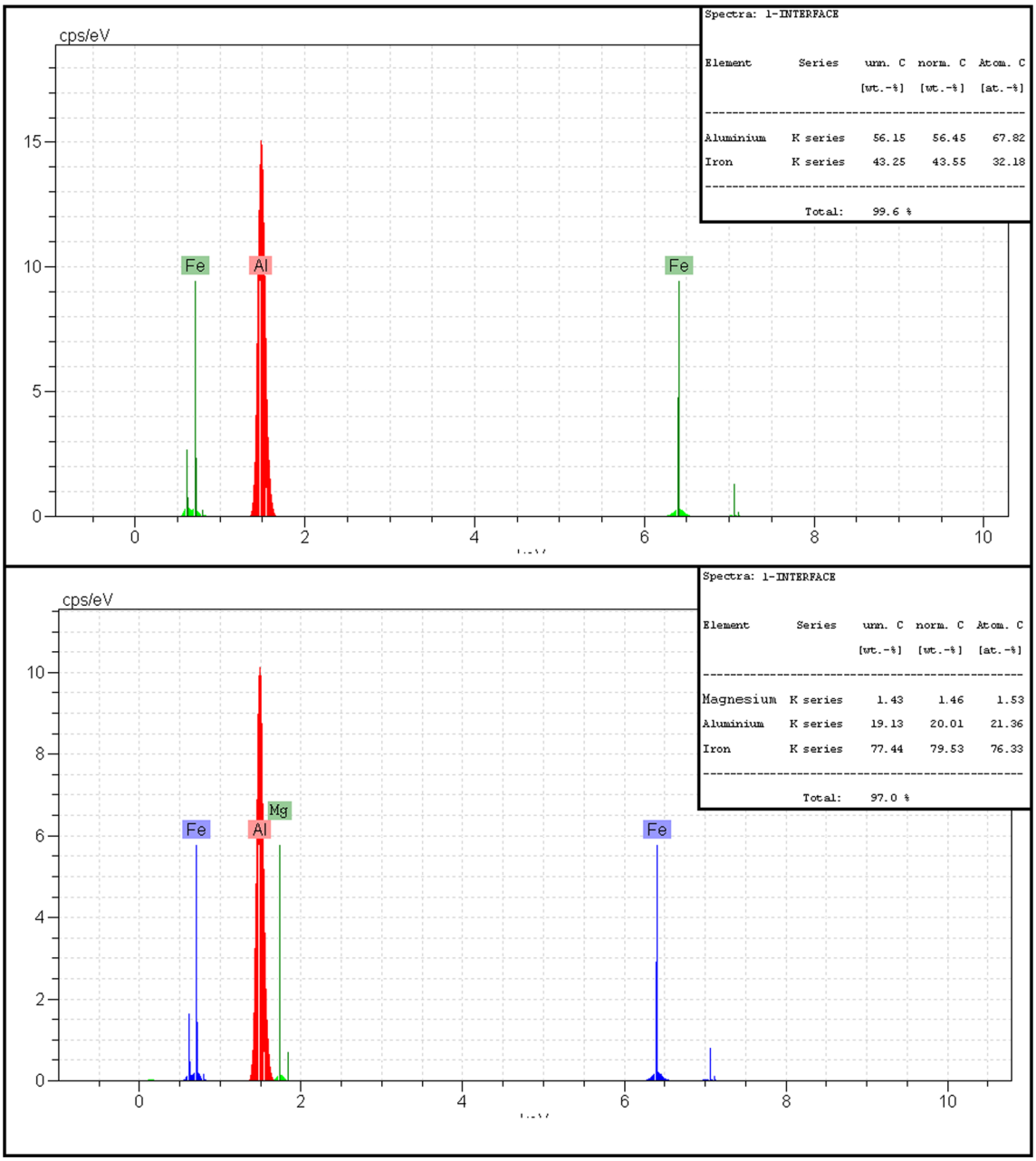

Fig. 13 EDS point-scan analysis results for the dissimilar welded joints at **a** $w = 1200$ and **b** $w = 1000$ rpm

toward the AA5005 alloy and St-52 steel sides on the transverse temperature profiles is demonstrated in Fig. 8. Analysis of these simulated contours reveals the formation of smaller HAZ and TMAZ regions with the lower peak temperature in the aluminum side as compared to the steel one under both processing conditions. In the case of Fig. 8a for the tool offset distance of 1.5 mm toward the steel side, the reason is obvious because of more volume fraction of rotating tool located in the steel which can leads to generation of more frictional heating, higher peak temperature, and formation of larger HAZ and TMAZ regions under this condition. In the other side by locating the rotating tool with an offset distance of 1.5 mm toward the aluminum part, the situation is less severe in Fig. 8b, but still, the temperature at the steel side is higher with larger HAZ and TMAZ regions. It is caused by the lower shear stress of aluminum as compared to the steel as well as its higher heat sinking capability due to higher thermal conductivity. As reported in the literature on this field [32–44], during dissimilar friction-stir joining of aluminum and steel materials always peak temperature at the steel side would be higher than the Al part that can induce the formation of larger HAZ and TMAZ regions. Also, it can be seen that by tool shifting toward the steel side, the temperature can increase even higher than the melting point of the aluminum sheet. However, offset toward the Al side can balance this matter. The same results about the effects of tool plunge depth (0.3 and 0.6 mm) at a constant offset distance on the transverse thermal contours are reported in Fig. 9a, b. It can be found that with increasing the tool plunge depth temperature profile can more extend due to more frictional heating and intensified plastic deformation. However, its influence is slight as compared to the distance and sequence of offsets. Figure 10 provides the predicted materials velocity, strain rate, materials distribution, and flow stress contours for top surface and thickness cross-section of a dissimilar friction-stir welded AA5005/St-52 joint. According to the simulation results, the velocity and strain rate fields at advancing side (aluminum side) is severe than the retreating one (steel side), although, this trend for pressure is vice versa. It is worth noting that the flow stress at advancing side around the SZ is compressive and gradually changes to tensile toward the retreating side and decreases by the distance from the welding center line. In the same trend with the predicted temperatures profiles, asymmetric nature of FSW process causes asymmetric variations for the pressure and velocity fields around the rotating FSW tool across the produced dissimilar joints [1, 2]. Since thermal analysis indicates the temperature profile at the Al-Fe interface (see Figs. 4, 5, 6, 7, 8, and 9) that can control the inter-diffusion of elements across the interface connected with the materials flow and inter-mixing patterns in Fig. 10 aided the solid-state deformation-assisted chemical reactions, these thermo-mechanical analysis results are very important for description of experimental results in the following sections.

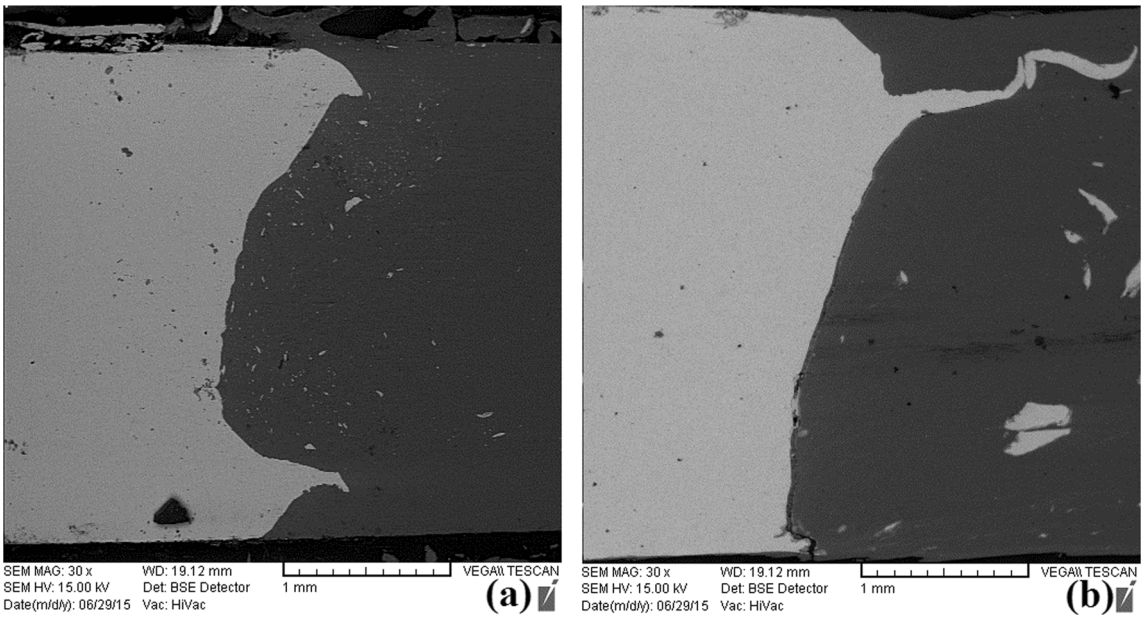

Fig. 14 FE-SEM macro-images showing the cross-sectional materials flow profiles for dissimilar FSW joints at different tool traverse velocities of **a** 54 and **b** 90 mm/min with a constant rotational speed of 1200 rpm

4.2 Effects of tool rotational speed

In Fig. 11, the cross-sectional FE-SEM macro-structures of two dissimilar friction-stir welds processed at two different w with a constant v are compared (Al side is shown as black contrast and steel side with gray contrast). A big tunneling defect can be seen at the aluminum side in the thickness section of dissimilar weld prepared at $w = 920$ rpm/$v = 54$ mm/min owing to less heat generation. Although, processing at higher rotational speed ($w = 1200$ rpm/$v = 54$ mm/min) leads to the formation of a sound defect-free dissimilar weld between AA5005 alloy and St-52 steel. It can be due to increasing the heat input by increasing w and its positive influence on the enhancement of materials flow pattern [1, 2, 59]. Furthermore, the fraction and size of steel fragments within the Al side are increased, as well. Effects of tool rotational speed at a constant traverse velocity on the size and morphology of IMC layer at the Al-Fe interface for upper and lower parts of dissimilar welded joints are presented in Fig. 12. As seen, considerable micro-scale metallurgical changes were occurred at the interface depending on the processing heat input. With increasing the tool rotational speed from 920 rpm up to 1200 rpm, the size of the IMC layer at

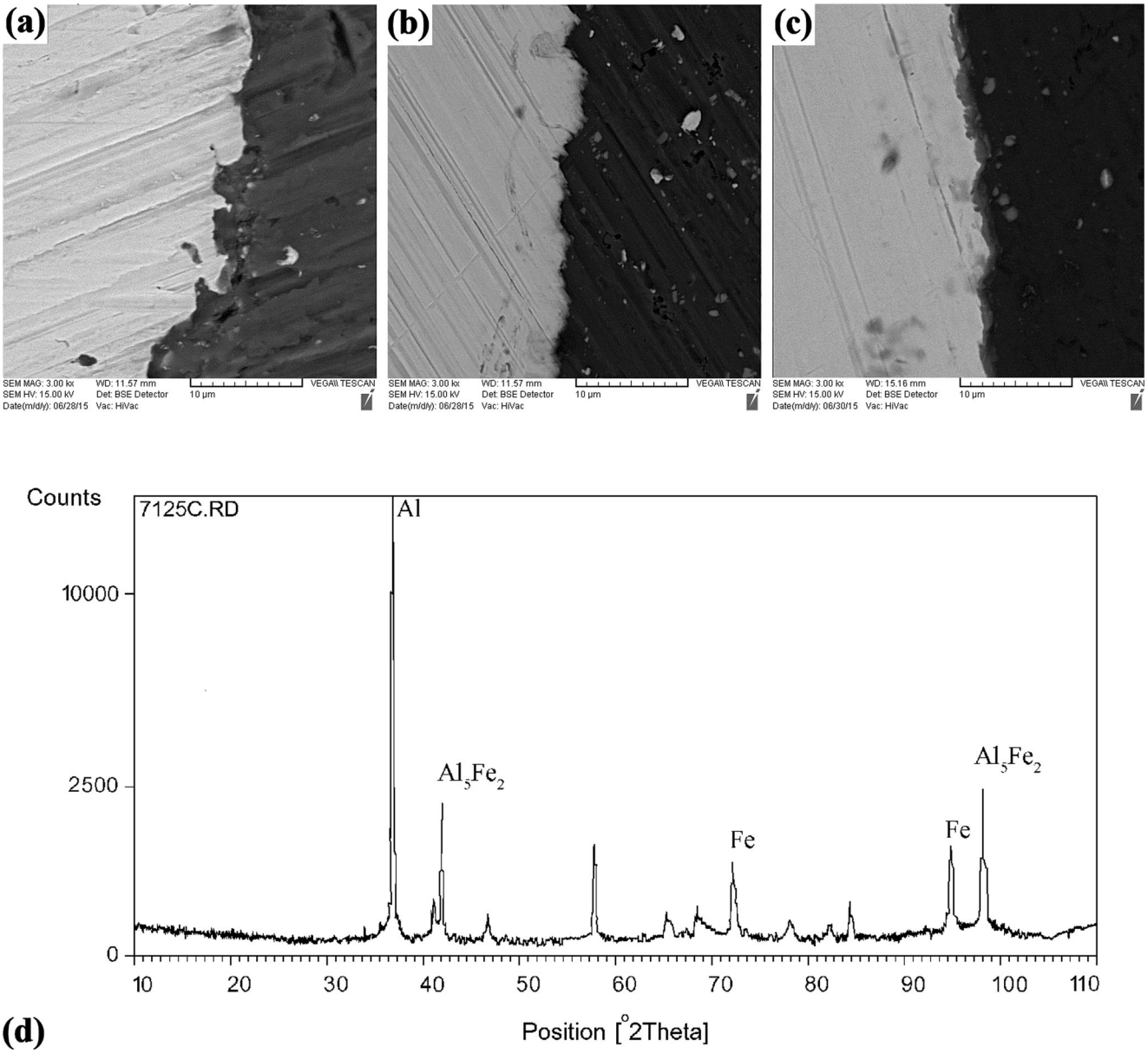

Fig. 15 FE-SEM images from the Al/Fe interfaces for the dissimilar welded joints at **a** $w = 920$, **b** $w = 1000$, and **c** $w = 1200$ rpm with $v = 90$ mm/min. **d** XRD pattern from the thickness cross-section of dissimilar FSW processed with $w = 1200$ rpm and $v = 90$ mm/min

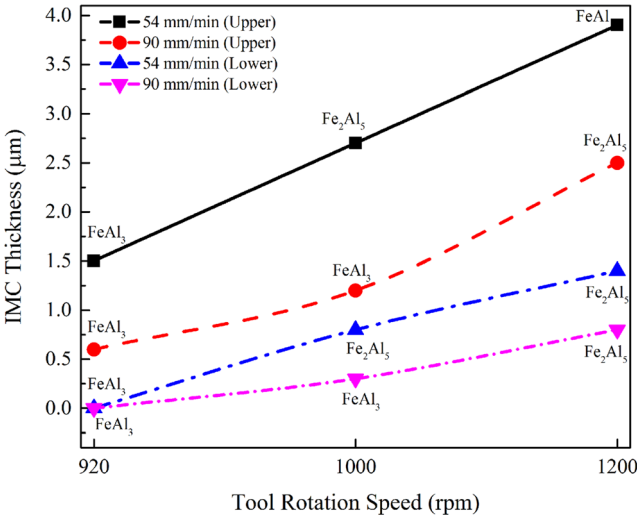

Fig. 16 Effects of tool rotational speed and traverse velocity on the thickness of IMC layer at the interface of the dissimilar joint between aluminum and steel

the interface is considerably increased. In addition to the IMC layer at the interface, some intermetallic compound particles (IMP) were detached from the interface during FSW process and dispersed within the metal matrix in the aluminum side, as induced by the stirring action of rotating tool. Also in the comparison between the upper and lower parts, for all conditions, the size of IMC layer in the lower part is thinner than the upper one due to less heat generation by keeping the distance from the rotating tool shoulder (compare Fig. 12a–c with d–f). Even in the lower part of the processed sample at $w = 920$ and 1000 rpm, there is not any detectable IMC layer at the interface (see Fig. 12d, e). As indexed by the EDS analysis in Fig. 13, these intermetallic compounds are mostly Fe rich, although the stoichiometry can be changed by the processing parameters and mainly heat input.

4.3 Effects of tool traverse velocity

FE-SEM images showing the cross-sectional macro-profiles from dissimilar materials flow pattern and inter-mixing for the dissimilar welds processed at two different traverse velocities are presented in Fig. 14. As shown, the influence of v is the same as w, considering its role in changing the w/v ratio and subsequently controlling the processing heat input. As a result, higher v can deteriorate the dissimilar joint formation. In comparison with Fig. 12, the same results are reported in Fig. 15a–c for the effects of w on the IMC layer at the interface, but at $v = 90$ mm/min. It can be found that by two times increasing of v, the formation of IMC layer at the interface is considerably suppressed due to kinetic aspects. As shown in Fig. 15d, XRD analysis was performed on the thickness cross-sections of dissimilar welded joints at different processing conditions to identify the type of intermetallic compounds at the interface. The results are reported in Fig. 16. It can be seen that the different intermetallics ($FeAl_3$, Fe_2Al_5, and FeAl) are produced depending on the employed w and v parameters as well as the distance from tool shoulder across the thickness section (upper/lower parts).

4.4 Effects of probe offset distance

The tool offset distance and sequence is one of the main parameters can control the IMC layer formation. Effects of tool offset distance toward the steel or aluminum sides and its magnitude on the formation of the dissimilar weld between AA5005 alloy and St-52 steel are shown in FE-SEM images of Fig. 17. Figure 17a shows the macro-structure of dissimilar welded joint with a 1.5-mm tool offset distance toward the steel side. Large C-shape contact interface area in this sample is due to high heat generation and partial melting

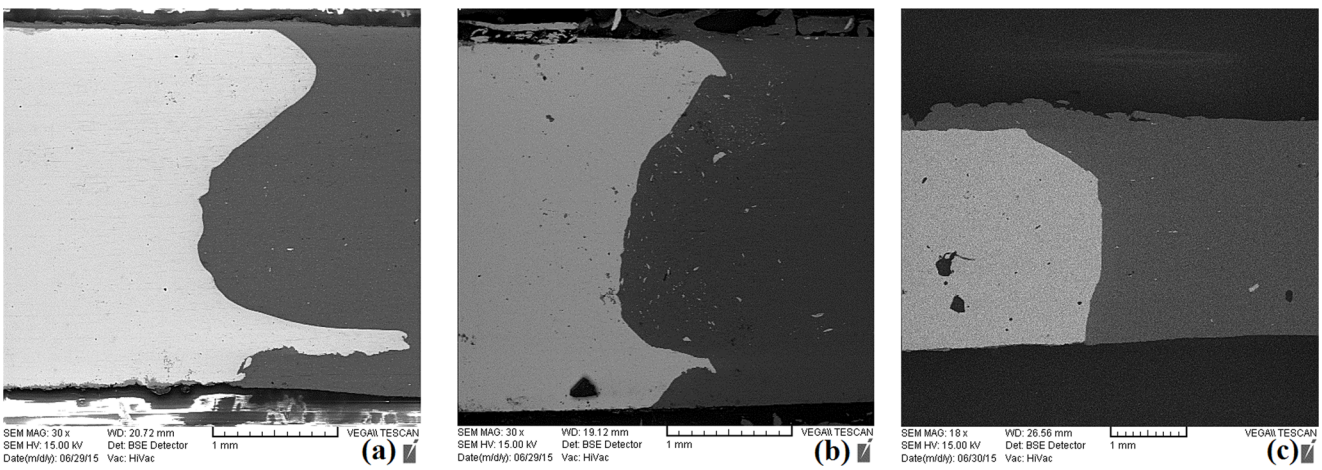

Fig. 17 FE-SEM macro-images showing the cross-sectional materials flow profiles for dissimilar FSW joints with **a** 1.5 mm offset toward the steel side, **b** 0.5, and **c** 1.5 mm offset toward the aluminum side

of the aluminum material. In Fig. 17b, c, these cross-sectional macro-profiles for 0.5 and 1.5 mm offset distances toward the aluminum side are presented. As shown in Fig. 17c, insufficient heat generation during the FSW process because of high offset distance toward the Al side leads to lock of inter-mixing between aluminum and steel materials, since the frictional heating was not enough for softening of the steel part. In the processed sample with a moderate 0.5 mm offset distance toward the Al side, some proper features related to the dissimilar materials inter-mixing and macro- and micro-mechanical inter-locking can be noticed. Figure 18 shows the high-magnification FE-SEM images from the Al-Fe interfaces for the processed dissimilar welds with 1.5 mm offset distance toward the Al and steel sides, respectively as combined with the related EDS analysis results. It can be found that offsetting toward the steel side caused by the generation of high heat input can lead to the formation of a large IMC layer at the interface. As indexed

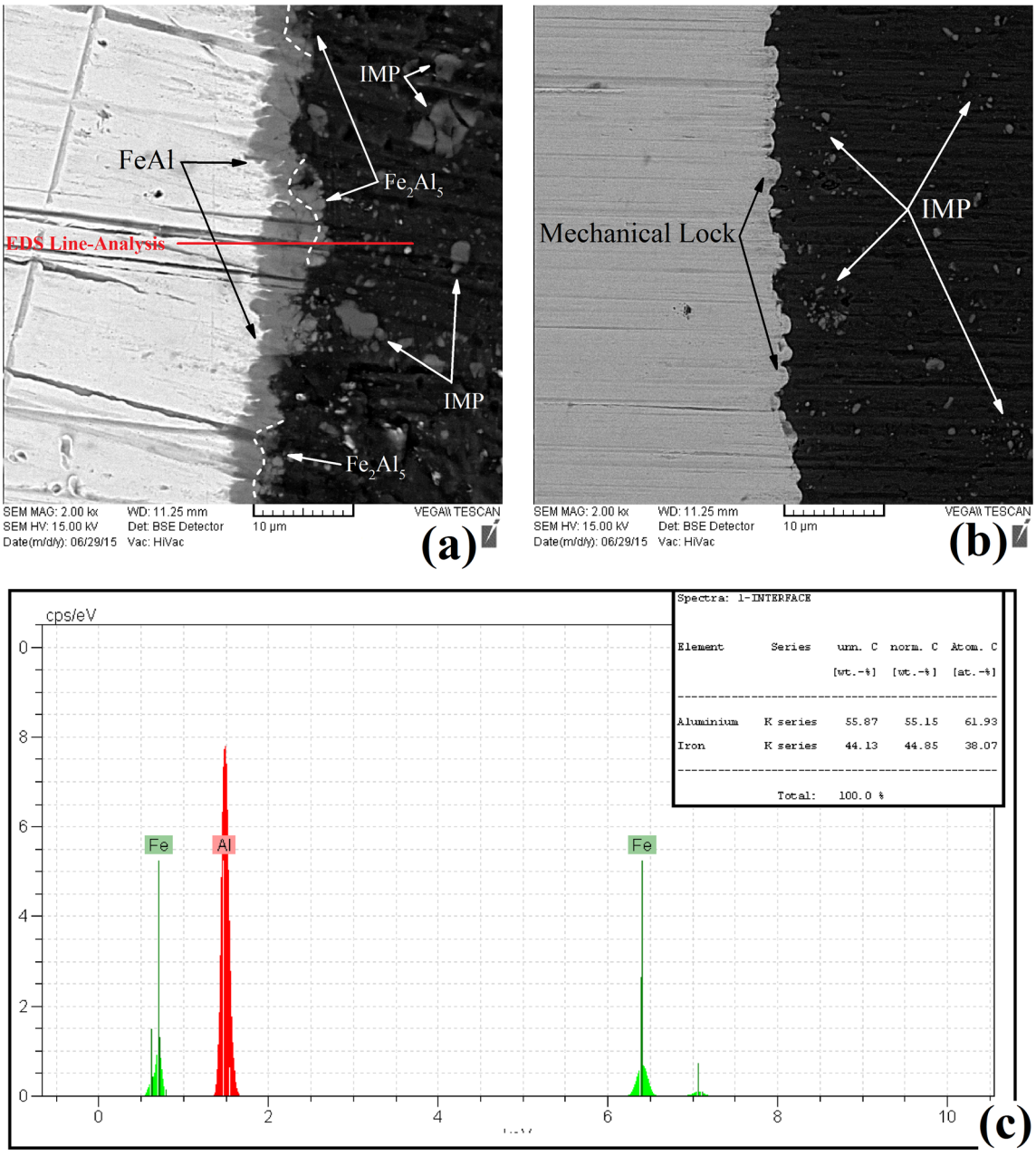

Fig. 18 Morphology of Al/Fe interface for dissimilar friction-stir welded joints with 1.5 mm tool offset distance toward the **a** steel and **b** aluminum sides, respectively. **c** EDS point scans analysis results from the Al/Fe interface

in Fig. 18a and also plotted in Fig. 19, two different types of intermetallics (FeAl and Fe_2Al_5) can be formed along the IMC layer with the thickness of ~ 10 μm. Although for the processed sample with 1.5 mm offset toward the Al side, there is not any evidence for the formation of IMC layer at the interface, and only some IMPs within the aluminum matrix and close to the interface are detectable. Based on these experiments and presented results, the tool offset distance as an important processing parameter can be optimized as a magnitude of ~ 0.5 mm with shifting toward the aluminum side for dissimilar butt-welding of AA5005 alloy and St-52 steel.

4.5 Effects of tool plunge depth

The same results about the influence of tool plunge depth on the formation of dissimilar FSW are reported in Figs. 20 and 21. For the processed sample with low plunge depth of 0.1 mm, a very thin IMC layer was formed at the Al-Fe interface (see Fig. 20a). It seems that this plunge depth was not enough for forging action of rotating tool to provide the superior dissimilar metals inter-mixing. In the high plunge depth sample of 0.6 mm, FE-SEM image of Fig. 20b shows the formation of a large IMC layer with the thickness of higher than 20 μm caused by imposing of high heat input as well as the severe shear deformation. According to the line-scan EDS analysis results in Fig. 21, three different compounds can be characterized inside the IMC layer, as FeAl, $FeAl_3$, and Fe_2Al_5. As explained, both of these extreme plunge depth values have some deteriorative influences. Therefore, the tool plunge depth as another effective processing parameter is optimized with a moderate value of ~ 0.3 mm.

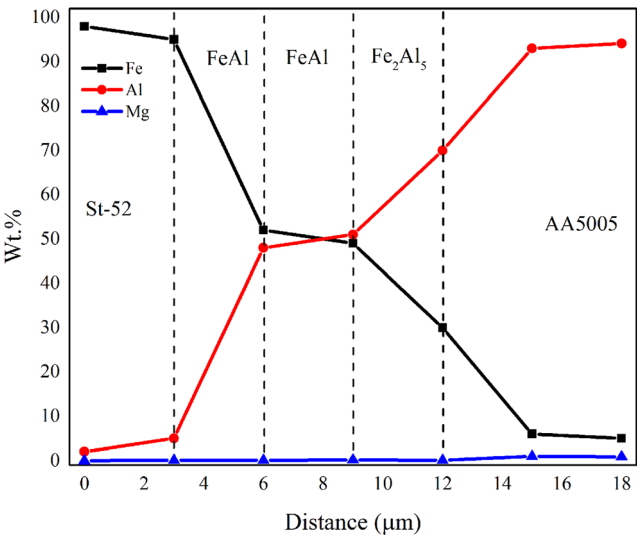

Fig. 19 The EDS line-scan analysis results from the Al/Fe interface

4.6 IMC layer formation and growth

As observed in the current research and also reported in literature before, feasibility of dissimilar friction-stir welding between aluminum alloys and steels and subsequent mechanical performance of processed dissimilar joints are strongly depended on the formation and morphological characteristics of IMC layer at the interface [13, 15–17, 21–23, 26, 33, 34, 36, 37, 42]. Frictional heating and deformation during the FSW process lead to the formation of various compositions of intermetallics depending on the processing conditions (see Fig. 16). Generally, it was reported that Al-rich intermetallics (such as $FeAl_3$ and Fe_2Al_5) are more brittle than the Fe-rich ones (such as FeAl and Fe_3Al) considering the mechanical property importance [11, 17, 23, 32, 40]. According to the thermodynamical stability viewpoint and Gibbs free energy of formation, Fe_3Al is the stablest phase among the different intermetallics in the Al-Fe system [11]. However, considering the kinetic aspects, $FeAl_3$ is the easiest phase to form in this system [20, 32, 49]. In the most of previous researches as well as the current study, formation of a two-phase reaction layer containing θ ($FeAl_3$) and η (Fe_2Al_5) phases was found dominant depending on the processing heat input (see Figs. 19 and 21) [17, 20, 27, 32, 34, 40, 45, 58]. Although, in the most thickness fraction of IMC layer, the η phase would be dominant [32]. As shown in Fig. 16, it can be seen that by increasing w and decreasing v (increscent of w/v ratio) composition is shifted toward the Fe-rich intermetallics, by changing the type from $FeAl_3$ into the Fe_2Al_5 and FeAl compounds, respectively. Considering the more brittleness of Al-rich intermetallics, this transition is favorable to enhance the mechanical performance of dissimilar Al-Fe friction-stir welds.

The formation and growth kinetics of the IMC layer at the Al-Fe interface is a diffusion-controlled phenomenon which can be described according to the below parabolic and Arrhenius relations [32]:

$$x^2 = kt = k_0 t \exp\left(\frac{-Q}{RT}\right) \tag{14}$$

where x is the thickness of IMC layer at the interface, k is the rate constant, t is the exposure time, k_0 is the pre-exponential factor, Q is the effective activation energy, R is the universal gas constant, and T is the processing temperature. Based on this state equation, all processing parameters or factors affecting the peak temperature or activation energy for diffusion of elements can affect the thickness or morphology of the IMC layer at the Al-Fe interface, as well. It is well-established in the literature [32, 40] that by increasing the tool rotational speed and reducing its traverse velocity, or increasing the w/v ratio, the heat input increases with the main impact result of

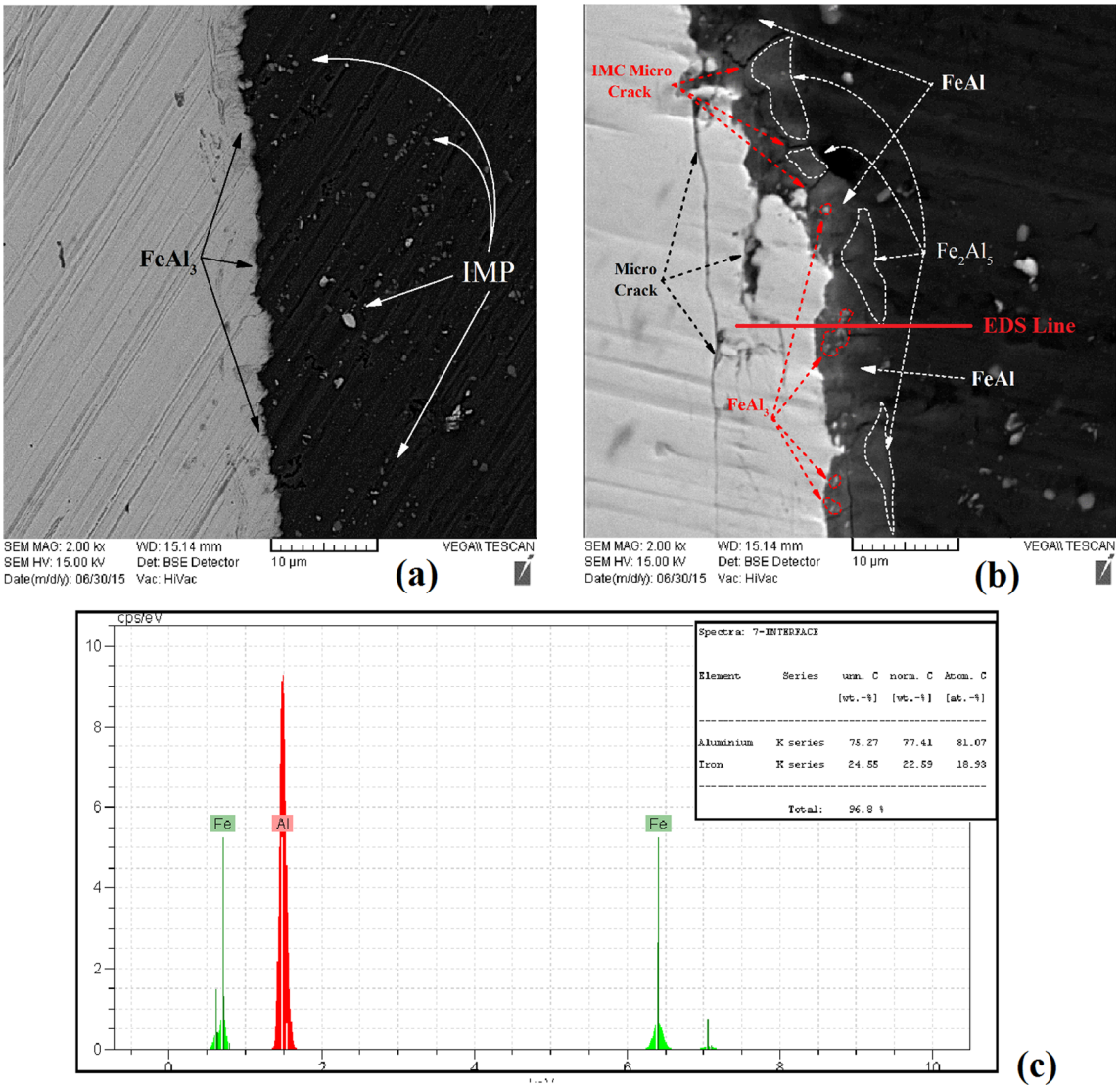

Fig. 20 Effects of **a** 0.1 and **b** 0.6 mm tool plunge depths on the locking morphology at the interface during FSW. **c** The EDS point-scan analysis results from the Al-Fe interface

increasing the peak temperature during process that can accelerate the inter-diffusion phenomena for different elements and subsequent formation of IMC layer at the interface. Therefore, increasing the heat input *w*/*v* index parameter (by increasing *w* or decreasing *v*) due to increasing the maximum temperature in the thermal cycle and lengthening the period time, i.e., *T* and *t* in the above equation, can cause the formation of thicker IMC layer. Furthermore, stirring action of the rotating tool during the FSW process can control the formation of IMC layer, as well. The main important factors as examined in this research were tool plunge depth and probe offset distance. Higher pressure and strain rate during the process as caused by frictional heating and shear deformation beside of enhanced materials inter-mixing can play an important role in making the easier paths for diffusion of elements. By reducing the effective activation energy, as a result, thicker IMC layer can form (see Figs. 19, 20, and 21). It is not yet well determined that the size of the IMC layer at the interface can play a role in detrimental or beneficial ways against the dissimilar weld strength [20, 27, 32, 40]. There is some paradox reports about that in the literature [15, 17–22, 26, 27, 29, 34, 35, 38, 40, 47]. Meanwhile, up to now, based on the findings of present research, it can admire that the examined processing parameters (*w*, *v*, plunge depth, and offset distance) displayed an impact influence on the composition, morphology, and thickness of IMC layer further than the soundness of weldments which can affect the mechanical performance of dissimilar welds, subsequently.

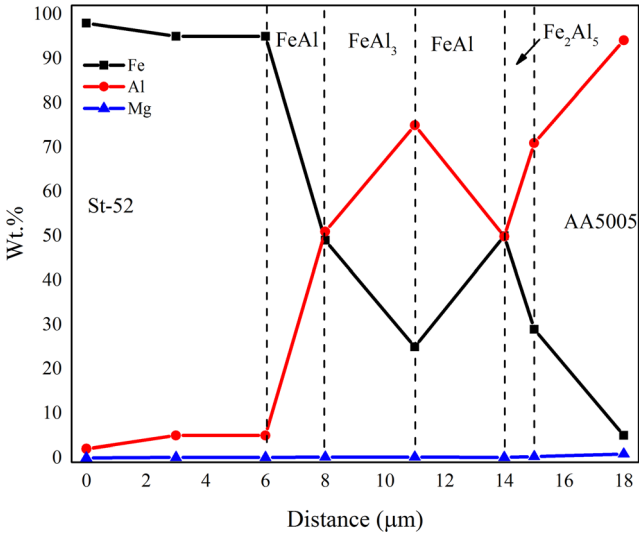

Fig. 21 The EDS line-scan analysis results from the Al/Fe interface with 0.6 mm tool plunge depth

4.7 Tensile strength and fracture behavior

Fracture behavior of dissimilar friction-stir welded joints at different processing parameters during transverse tensile testing is compared in Fig. 22. As shown, different fracture locations depending on the employed processing conditions can be observed. The occurrence of transverse failure outside of the weld nugget indicates the joint mechanical satisfaction. It can be seen that some processed dissimilar joints were fractured from the HAZ and TMAZ regions in the aluminum side. For the failed samples from SZ, as shown in Fig. 23, the size and morphology of the IMC layer at the interface play a major role in the corresponding fractographic aspects. By increasing the thickness size of the IMC layer, fracture tends toward the catastrophic nature. In Fig. 24a, b, macro-images from two aluminum and steel failure sides are presented for the optimized dissimilar weld at processing parameters of $w =$ 1200 rpm and $v = 90$ mm/min with failure location from HAZ of Al side. Behavior is close to ductile rupture with a shear edge of around 45°. The joining efficiency, as defined by the tensile strength ratio of the dissimilar joint to the aluminum base metal, was determined for the processed dissimilar joints by considering their transverse tensile rupture curves. Effects of tool rotation speed, traverse velocity, offset distance, and plunge depth on the joining efficiency of processed dissimilar joints are plotted and compared in Fig. 24c–e. Trends of evolution have some optimums. As explained before, changing in the processing conditions mainly can affect the IMC layer formation at the interface, as well as the materials flow pattern, inter-mixing, and mechanical locking mechanisms. However, the presence of the IMC layer at the interface and its size and morphology are the key factors which can control the tensile flow behavior of processed dissimilar joints. Therefore, a correlation between the IMC layer formation and joining efficiency depending on the processing heat input can be established. Based on the presented data in Fig. 24, processing parameters can be optimized as $w = 1200$ rpm, $v = 90$ mm/min, tool offset distance of 0.5 mm toward the Al side, and tool plunge depth of 0.3 mm with the highest joining efficiency of ~ 90%.

4.8 Indentation micro-hardness

The Vickers micro-hardness profiles across the thickness section of processed dissimilar FSWs from different parts at two high (1200 rpm) and low (920 rpm) tool rotational speeds are compared in Fig. 25a, b, respectively. As seen, the average hardness values for aluminum alloy and low carbon steel base metals are ~ 70 and 220 HV, respectively. The hardness of mixed nugget can be changed by formation of IMC layer at the interface depending on the processing heat input. For low w processed weld, the hardness increscent for the SZ is not considerable (~ 200 HV). Despite less IMC fraction, this strengthening amount can be due to the presence of IMPs [63–65]. By increasing w and subsequently increasing heat input which can accelerate the IMC layer formation, the hardness at SZ region is enhanced up to ~ 250 HV (see Fig. 25a).

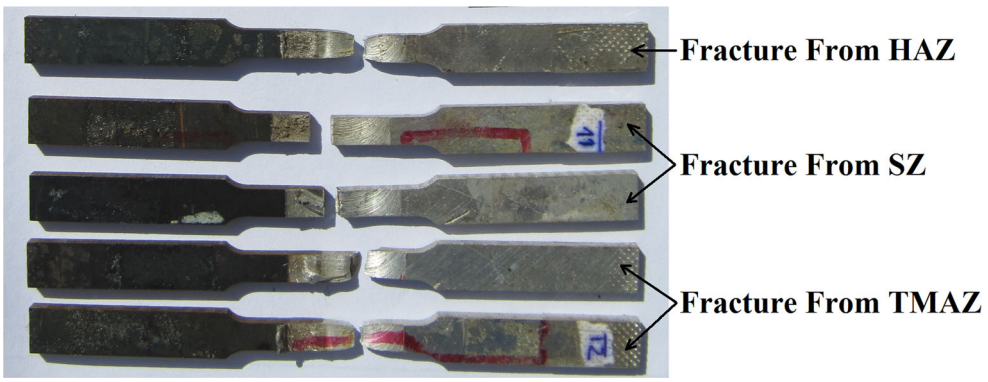

Fig. 22 Top-view of transverse tensile failed samples

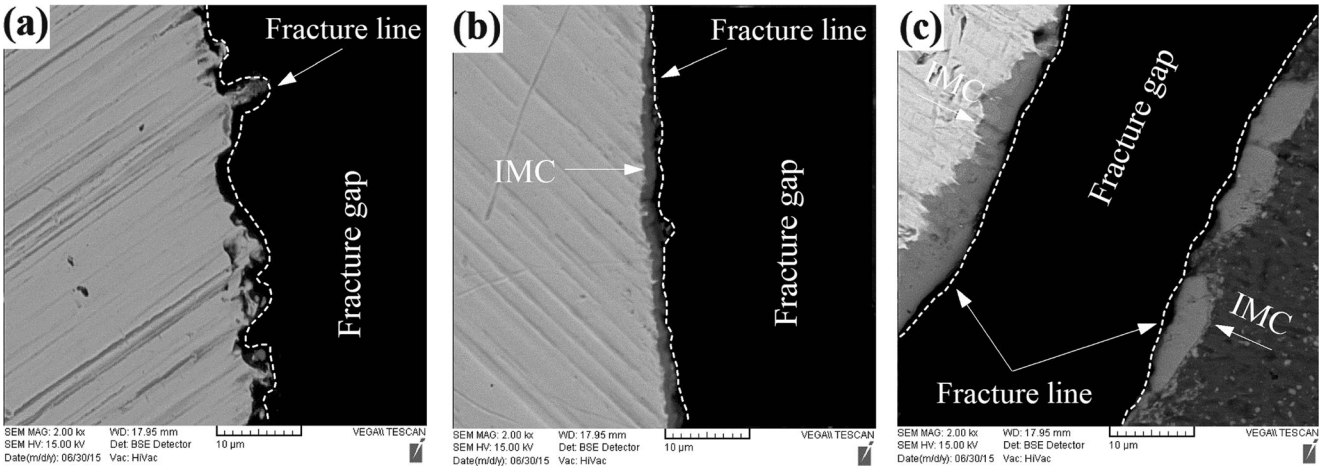

Fig. 23 The fracture interfaces for dissimilar joints **a** without IMC layer, **b** low thickness of the IMC layer, and **c** high thickness of the IMC layer

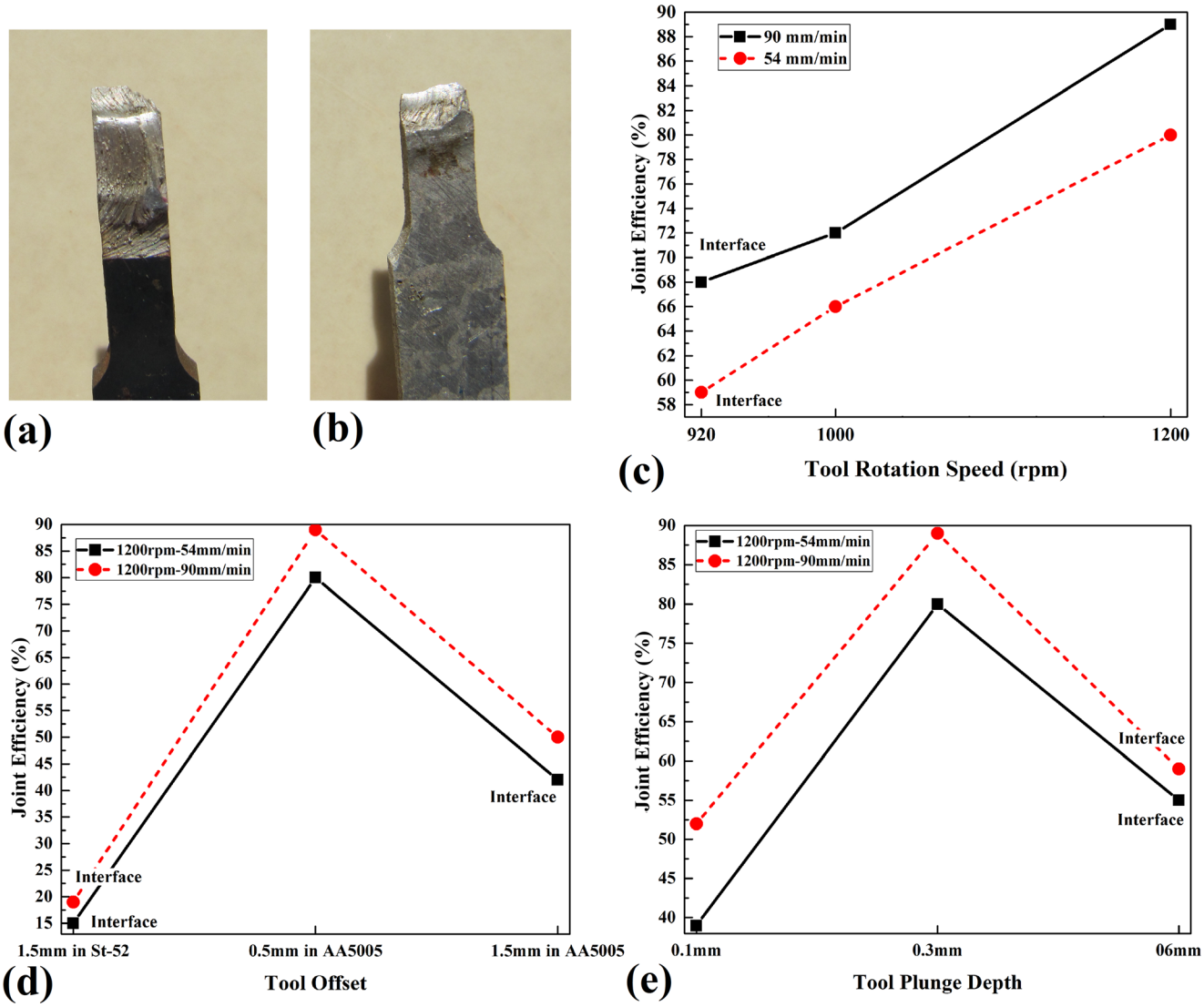

Fig. 24 Macro-images from the fracture surfaces of dissimilar joint with highest efficiency for the **a** St-52 and **b** AA5005 sides. Effects of **c** tool rotational speed, traverse velocity, **d** tool offset, and **e** tool plunge depth on the joining efficiency for dissimilar FSW of St-52 and AA5005 sheets

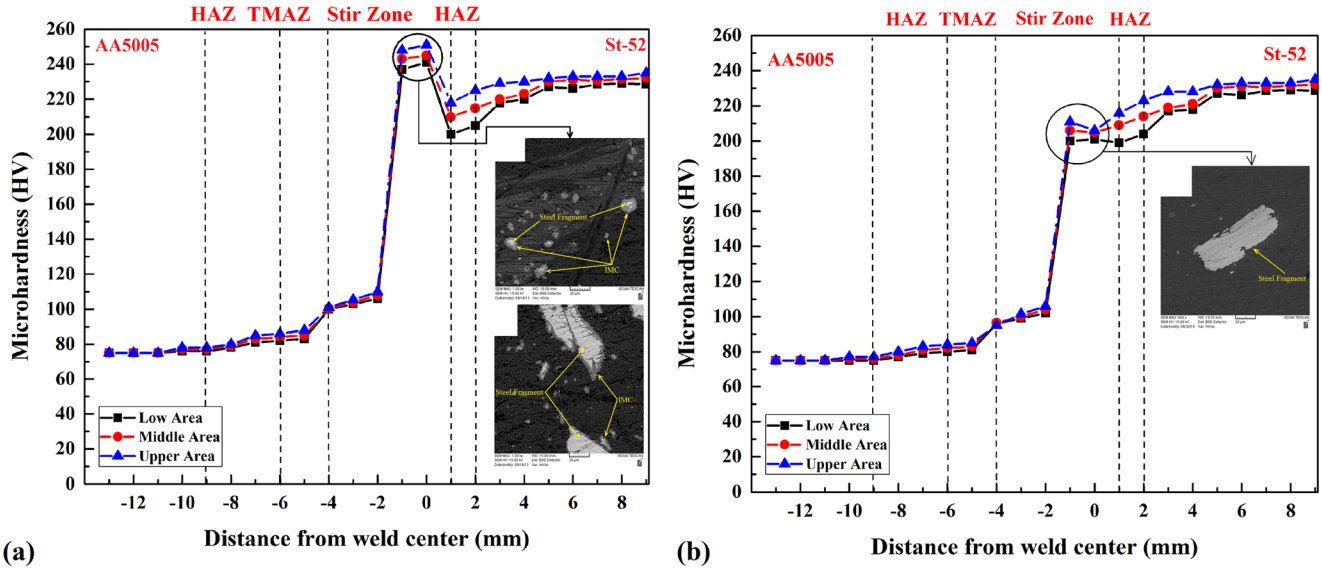

Fig. 25 Effects of tool rotational speed on the micro-hardness profiles across the thickness section of processed dissimilar joints at different regions; **a** $w = 1200$ rpm and **b** $w = 920$ rpm

5 Conclusions

Dissimilar weldability of AA5005-O aluminum-magnesium alloy and St-52 low carbon steel in a butt-joint design in terms of IMCs layer formation at the interface depending on the main processing parameters (w, v, tool plunge depth, and tool offset distance) was thermo-mechanically modeled and experimentally elaborated. The main findings can be expressed as follows:

- According to the simulation results, as validated by experimental testing, tool offset distance toward the steel sheet can cause the melting of aluminum material. By increasing w, decreasing v, and increasing tool plunge depth (i.e., higher heat input), the peak temperature was continuously improved up to ~ 853 K with the enhanced materials flow pattern.
- The higher peak temperatures during FSW process intensified the growth kinetics of IMC layer at the interface, as well as its formation and morphology which mainly influenced by the dissimilar materials inter-mixing profile as induced by the processing conditions (w/v ratio). Different FeAl and Fe_2Al_5 intermetallics were formed in a thickness range of < 20 μm.
- To fabricate a sound dissimilar butt-joint between these dissimilar materials based on the formation of defects across the weld and IMC layer at the interface, processing parameters were optimized as $w = 1200$ rpm and $v = 90$ mm/min, with tool plunge depth of 0.3 mm by locating the Al sheet at advancing side with a tool offset distance of 0.5 mm toward this Al part.
- For sound/defect-free dissimilar welds, the lower thickness of the IMC layer can enhance the dissimilar weld mechanical performance. Fracture of the optimized dissimilar weld occurred from the HAZ of Al side with a maximum joint efficiency of ~ 90%.
- The hardness of dissimilar mixed zone was strongly affected by the formation of IMC layer at the interface depending on the processing heat input. A maximum hardness increscent of ~ 250 HV was noticed as compared to ~ 70 and 220 HV for the aluminum and steel base metals, respectively.

6 Direction for future researches

Coupling the thermal and strain results of FEM modeling with the micro-scale statistical and diffusion-based models to predict the morphology and growth kinetics of IMC layer at the interface during FSW bonding is a critical phenomenon in determining the mechanical performance of produced dissimilar joints. Furthermore, the results can be experimentally verified by the implementation of scanning (STEM) and high-resolution transmission electron microscopy (HR-TEM) analyses from the interface of dissimilar bonded aluminum and steel, as well as the electron probe micro-analysis (EPMA) and Auger spectroscopy (AS). Although in this study it was tried out to analyze the effects of processing parameters comprehensively, some aspects about the effects of this IMC layer formation between aluminum and steel during dissimilar FSW joining on the correlation with the practical mechanical performance of produced components, such as fatigue, fracture and crack propagation, and toughness, must be studied in the future researches.

References

1. Mishra RS, Ma ZY (2005) Friction stir welding and processing. Mater Sci Eng R 50(1–2):1–78
2. Nandan R, DebRoy T, Bhadeshia HKDH (2008) Recent advances in friction-stir welding—process, weldment structure and properties. Prog Mater Sci 53(6):980–1023
3. Martinez N, Kumar N, Mishra RS, Doherty KJ (2017) Microstructural variation due to heat gradient of a thick friction stir welded aluminum 7449 alloy. J Alloys Compd 713:51–63
4. Tang J, Shen Y (2016) Numerical simulation and experimental investigation of friction stir lap welding between aluminum alloys AA2024 and AA7075. J Alloys Compd 666:493–500
5. Khodabakhshi F, Haghshenas M, Chen J, Shalchi Amirkhiz B, Li J, Gerlich A (2016) Bonding mechanism and interface characterisation during dissimilar friction stir welding of an aluminium/polymer bi-material joint. Sci Technol Weld Join 1–9
6. Khan NZ, Siddiquee AN, Khan ZA, Mukhopadhyay AK (2017) Mechanical and microstructural behavior of friction stir welded similar and dissimilar sheets of AA2219 and AA7475 aluminium alloys. J Alloys Compd 695:2902–2908
7. Rafiei R, Shamanian M, Fathi M, Khodabakhshi F (2017) Dissimilar friction-stir lap-welding of aluminum-magnesium (AA5052) and aluminum-copper (AA2024) alloys: microstructural evolution and mechanical properties. Int J Adv Manuf Technol:1–18
8. Khodabakhshi F, Ghasemi Yazdabadi H, Kokabi AH, Simchi A (2013) Friction stir welding of a P/M Al–Al_2O_3 nanocomposite: microstructure and mechanical properties. Mater Sci Eng A 585: 222–232
9. Khodabakhshi F, Simchi A, Kokabi AH, Gerlich AP (2016) Similar and dissimilar friction-stir welding of an PM aluminum-matrix hybrid nanocomposite and commercial pure aluminum: microstructure and mechanical properties. Mater Sci Eng A 666:225–237
10. Khodabakhshi F, Haghshenas M, Sahraeinejad S, Chen J, Shalchi B, Li J, Gerlich AP (2014) Microstructure-property characterization of a friction-stir welded joint between AA5059 aluminum alloy and high density polyethylene. Mater Charact 98:73–82
11. Lee IS, Kao PW, Ho NJ (2008) Microstructure and mechanical properties of Al-Fe *in situ* nanocomposite produced by friction stir processing. Intermetallics 16(9):1104–1108
12. Ding Y, Shen Z, Gerlich AP (2017) Refill friction stir spot welding of dissimilar aluminum alloy and AlSi coated steel. J Manuf Process 30:353–360
13. Hsieh MJ, Lee RT, Chiou YC (2017) Friction stir spot fusion welding of low-carbon steel to aluminum alloy. J Mater Process Technol 240:118–125
14. Huang Y, Wang J, Wan L, Meng X, Liu H, Li H (2016) Self-riveting friction stir lap welding of aluminum alloy to steel. Mater Lett 185: 181–184
15. Piccini JM, Svoboda HG (2017) Tool geometry optimization in friction stir spot welding of Al-steel joints. J Manuf Process 26: 142–154
16. Haghshenas M, Abdel-Gwad A, Omran AM, Gökçe B, Sahraeinejad S, Gerlich AP (2014) Friction stir weld assisted diffusion bonding of 5754 aluminum alloy to coated high strength steels. Mater Des 55:442–449
17. Leitao C, Arruti E, Aldanondo E, Rodrigues DM (2016) Aluminium-steel lap joining by multipass friction stir welding. Mater Des 106:153–160
18. Liu X, Lan S, Ni J (2014) Analysis of process parameters effects on friction stir welding of dissimilar aluminum alloy to advanced high strength steel. Mater Des 59:50–62
19. Ramachandran KK, Murugan N, Shashi Kumar S (2015) Effect of tool axis offset and geometry of tool pin profile on the characteristics of friction stir welded dissimilar joints of aluminum alloy AA5052 and HSLA steel. Mater Sci Eng A 639:219–233
20. Pourali M, Abdollah-zadeh A, Saeid T, Kargar F (2017) Influence of welding parameters on intermetallic compounds formation in dissimilar steel/aluminum friction stir welds. J Alloys Compd 715:1–8
21. Yazdipour A, Heidarzadeh A (2016) Effect of friction stir welding on microstructure and mechanical properties of dissimilar Al 5083-H321 and 316L stainless steel alloy joints. J Alloys Compd 680: 595–603
22. Tang J, Shen Y (2017) Effects of preheating treatment on temperature distribution and material flow of aluminum alloy and steel friction stir welds. J Manuf Process 29(Supplement C):29–40
23. Rafiei R, Moghaddam AO, Hatami M, Khodabakhshi F, Abdolahzadeh A, Shokuhfar A (2017) Microstructural characteristics and mechanical properties of the dissimilar friction-stir butt welds between an Al–Mg alloy and A316L stainless steel. Int J Adv Manuf Technol 90(9–12):2785–2801
24. Fei X, Jin X, Ye Y, Xiu T, Yang H (2016) Effect of pre-hole offset on the property of the joint during laser-assisted friction stir welding of dissimilar metals steel and aluminum alloys. Mater Sci Eng A 653:43–52
25. Khodabakhshi F, Kokabi A, Simchi A (2017) Reactive friction-stir processing of nanocomposites: effects of thermal history on microstructure–mechanical property relationships, Mater Sci Technol 1–14
26. Zheng Q, Feng X, Shen Y, Huang G, Zhao P (2016) Dissimilar friction stir welding of 6061 Al to 316 stainless steel using Zn as a filler metal. J Alloys Compd 686:693–701
27. Dehghani M, Amadeh A, Akbari Mousavi SAA (2013) Investigations on the effects of friction stir welding parameters on intermetallic and defect formation in joining aluminum alloy to mild steel. Mater Des 49(Supplement C):433–441
28. Elyasi M, Aghajani Derazkola H, Hosseinzadeh M (2016) Investigations of tool tilt angle on properties friction stir welding of A441 AISI to AA1100 aluminium. Proc Inst Mech Eng B J Eng Manuf 230(7):1234–1241
29. Derazkola HA, Aval HJ, Elyasi M (2015) Analysis of process parameters effects on dissimilar friction stir welding of AA1100 and A441 AISI steel. Sci Technol Weld Join 20(7):553–562
30. Sawada YK, Nakamura M (2013) Lapped friction stir welding between ductile cast irons and stainless steels. Weld Int 27(2): 121–128
31. Khodabakhshi F, Simchi A, Kokabi A, Gerlich A, Nosko M, Švec P (2017) Influence of hard inclusions on microstructural characteristics and textural components during dissimilar friction-stir welding of an PM Al–Al_2O_3–SiC hybrid nanocomposite with AA1050 alloy. Sci Technol Weld Join 22(5):412–427
32. Xu L, Robson JD, Wang L, Prangnell PB (2017) The influence of grain structure on intermetallic compound layer growth rates in Fe-Al dissimilar welds. Metall Mater Trans A
33. Chen CM, Kovacevic R (2004) Joining of Al 6061 alloy to AISI 1018 steel by combined effects of fusion and solid state welding. Int J Mach Tools Manuf 44(11):1205–1214
34. Elrefaey A, Gouda M, Takahashi M, Ikeuchi K (2005) Characterization of aluminum/steel lap joint by friction stir welding. J Mater Eng Perform 14(1):10–17
35. Uzun H, Dalle Donne C, Argagnotto A, Ghidini T, Gambaro C (2005) Friction stir welding of dissimilar Al 6013-T4 to X5CrNi18-10 stainless steel. Mater Des 26(1):41–46

36. Watanabe T, Takayama H, Yanagisawa A (2006) Joining of aluminum alloy to steel by friction stir welding. J Mater Process Technol 178(1):342–349
37. Chen T (2009) Process parameters study on FSW joint of dissimilar metals for aluminum–steel. J Mater Sci 44(10):2573–2580
38. Dehghani M, Mousavi SAAA, Amadeh A (2013) Effects of welding parameters and tool geometry on properties of 3003-H18 aluminum alloy to mild steel friction stir weld. Trans Nonferrous Metals Soc China 23(7):1957–1965
39. Liu X, Lan S, Ni J (2014) Analysis of process parameters effects on friction stir welding of dissimilar aluminum alloy to advanced high strength steel. Mater Des 59(Supplement C):50–62
40. Ratanathavorn W, Melander A, Magnusson H (2016) Intermetallic compounds in friction stirred lap joints between AA5754/galvanised ultra-high strength steel. Sci Technol Weld Join 21(8):653–659
41. Leitao C, Arruti E, Aldanondo E, Rodrigues DM (2016) Aluminium-steel lap joining by multipass friction stir welding. Mater Des 106(Supplement C):153–160
42. Dong H, Chen S, Song Y, Guo X, Zhang X, Sun Z (2016) Refilled friction stir spot welding of aluminum alloy to galvanized steel sheets. Mater Des 94(Supplement C):457–466
43. Zheng Q, Feng X, Shen Y, Huang G, Zhao P (2016) Dissimilar friction stir welding of 6061 Al to 316 stainless steel using Zn as a filler metal. J Alloys Compd 686(Supplement C):693–701
44. Huang Y, Wang J, Wan L, Meng X, Liu H, Li H (2016) Self-riveting friction stir lap welding of aluminum alloy to steel. Mater Lett 185(Supplement C):181–184
45. Jamshidi Aval H (2015) Microstructure and residual stress distributions in friction stir welding of dissimilar aluminium alloys. Mater Des 87:405–413
46. Jamshidi Aval H, Serajzadeh S, Sakharova NA, Kokabi AH, Loureiro A (2012) A study on microstructures and residual stress distributions in dissimilar friction-stir welding of AA5086-AA6061. J Mater Sci 47(14):5428–5437
47. Choi DH, Ahn BW, Lee CY, Yeon YM, Song K, Jung SB (2011) Formation of intermetallic compounds in Al and Mg alloy interface during friction stir spot welding. Intermetallics 19(2):125–130
48. Choi DH, Ahn BW, Quesnel DJ, Jung SB (2013) Behavior of β phase (Al_3Mg_2) in AA 5083 during friction stir welding. Intermetallics 35:120–127
49. Esmaeili A, Zareie Rajani HR, Sharbati M, Givi MKB, Shamanian M (2011) The role of rotation speed on intermetallic compounds formation and mechanical behavior of friction stir welded brass/aluminum 1050 couple. Intermetallics 19(11):1711–1719
50. Galvão I, Oliveira JC, Loureiro A, Rodrigues DM (2012) Formation and distribution of brittle structures in friction stir welding of aluminium and copper: influence of shoulder geometry. Intermetallics 22:122–128
51. Khodabakhshi F, Marzbanrad B, Shah L, Jahed H, Gerlich A (2017) Friction-stir processing of a cold sprayed AA7075 coating layer on the AZ31B substrate: structural homogeneity, microstructures and hardness. Surf Coat Technol 331:116–128
52. Khodabakhshi F, Simchi A, Kokabi A (2017) Surface modifications of an aluminum-magnesium alloy through reactive stir friction processing with titanium oxide nanoparticles for enhanced sliding wear resistance. Surf Coat Technol 309:114–123
53. Khodabakhshi F, Simchi A, Kokabi AH, Gerlich AP (2015) Friction stir processing of an aluminum-magnesium alloy with pre-placing elemental titanium powder: *in-situ* formation of an Al_3Ti-reinforced nanocomposite and materials characterization. Mater Charact 108:102–114
54. Cole GS, Sherman AM (1995) Light weight materials for automotive applications. Mater Charact 35(1):3–9
55. Hussein SA, Tahir ASM, Hadzley AB (2015) Characteristics of aluminum-to-steel joint made by friction stir welding: a review. Mater Today Commun 5:32–49
56. Jamshidi Aval H, Serajzadeh S, Kokabi AH, Loureiro A (2011) Effect of tool geometry on mechanical and microstructural behaviours in dissimilar friction stir welding of AA 5086-AA 6061. Sci Technol Weld Join 16(7):597–604
57. Zhang J, Shen Y, Li B, Xu H, Yao X, Kuang B, Gao J (2014) Numerical simulation and experimental investigation on friction stir welding of 6061-T6 aluminum alloy. Mater Des 60:94–101
58. Zhu X, Chao Y (2004) Numerical simulation of transient temperature and residual stresses in friction stir welding of 304L stainless steel. J Mater Process Technol 146(2):263–272
59. Nandan R, Roy GG, Lienert TJ, Debroy T (2007) Three-dimensional heat and material flow during friction stir welding of mild steel. Acta Mater 55(3):883–895
60. Rituraj Nandan (2008) Phd thesis, Computational modeling of heat transfer and visco-elastic flow in friction stir welding. The Pennsylvania State University
61. Amit Arora (2011) Phd thesis, Thermomechanical conditions and stresses on the friction stir welding tool. The Pennsylvania State University The Graduate School
62. Gale WF, Totemeier TC (2004) Smithells metals reference book. 8th ed. Elsevier Inc. All rights reserved
63. Khodabakhshi F, Arab S, Švec P, Gerlich A (2017) Fabrication of a new Al-Mg/graphene nanocomposite by multi-pass friction-stir processing: dispersion, microstructure, stability, and strengthening. Mater Charact 132:92–107
64. Khodabakhshi F, Gerlich AP, Švec P (2017) Fabrication of a high strength ultra-fine grained Al-Mg-SiC nanocomposite by multi-step friction-stir processing. Mater Sci Eng A 698:313–325
65. Khodabakhshi F, Gerlich AP, Švec P (2017) Reactive friction-stir processing of an Al-Mg alloy with introducing multi-walled carbon nano-tubes (MW-CNTs): microstructural characteristics and mechanical properties. Mater Charact 131:359–373